Correspondence to:
M. Rohanizadegan,
mrohanizadegan@uwaterloo.ca

High-Resolution Large-Eddy Simulations of Flow in the Complex Terrain of the Canadian Rockies

Mina Rohanizadegan[1], Richard M. Petrone[1], John W. Pomeroy[2], Branko Kosovic[3], Domingo Muñoz-Esparza[3], and Warren D. Helgason[4]

[1]Department of Geography and Environmental Management, University of Waterloo, Waterloo, ON, Canada, [2]Centre for Hydrology, University of Saskatchewan, Canmore, AB, Canada, [3]National Center for Atmospheric Research, Boulder, CO, USA, [4]Department of Civil, Geological, and Environmental Engineering, University of Saskatchewan, Saskatoon, SK, Canada

Abstract Improving the calculation of land-atmosphere fluxes of heat and water vapor in mountain terrain requires better resolution of thermally driven diurnal winds (i.e., valley, slope winds) due to differential heating by terrain and radiative fluxes. In this study, the Weather Research and Forecasting model is used to simulate flow in large-eddy simulation (LES) mode over the complex terrain of the Fortress Mountain and Marmot Creek research basins, Kananaskis Valley, Canadian Rockies, Alberta in mid-summer. The model was used to examine the temporal and spatial evolution of local winds and near-surface boundary layer processes with variability in topography and elevation. Numerically resolving complex terrain wind flow effects require smaller grid cell size. However, the use of terrain-following coordinates in most numerical weather prediction models results in large numerical errors when flow over steep terrain is simulated. These errors propagate through the domain and can result in numerical instability. To avoid this issue when simulating flow over steep terrain a local smoothing approach was used, where smoothing is applied only where slope exceeds some predetermined threshold. LES results from local smoothing were compared with a mesoscale model and LES with global smoothing. Simulations are evaluated using sounding data and meteorological stations. The differences in flow patterns and reversals in two mountain basins suggest that valley geometry and volume is relevant to the break up of inversion layers, removal of cold-air pools, and strength of thermally driven winds.

1. Introduction

Mountains interact with the atmosphere primarily through the atmospheric boundary layer (ABL) that extends up to a few km above ground level (AGL). Mountainous terrain is frequently exposed to topographic wind flows, which are produced by orographic lift of incoming mesoscale and strong prevailing winds (Whiteman, 2000). Under weak synoptic conditions thermally driven flows are also a common phenomenon in mountainous terrain, and are generated by horizontal contrasts in heating and cooling that arise from horizontal differences in temperature of the land and atmosphere due to diurnal differences in insolation (Lehner & Rotach, 2018; Serafin et al., 2018). These thermally induced flows are responsible for generating slope and valley flows (Rotach et al., 2015; Schmidli & Rotunno, 2010), and can develop different flow characteristics depending on the geometry of valleys and surrounding topography (Wagner et al., 2015).

Predictions of surface phenomena in mountains are affected by complex orography, and is identified as a challenge for numerical modeling. Many attempts have occurred in recent years to improve the accuracy of numerical weather prediction (NWP) models to resolve flow in mountainous terrain by increasing grid resolution (e.g., Goger et al., 2018; Udina et al., 2017; Vionnet et al., 2015), applying high-resolution land use and orography (Golzio et al., 2021; Jimenez-Esteve et al., 2018; Kalverla et al., 2016), or improving soil moisture representation (Chow et al., 2006). Weigel et al. (2007) modeled the contributing factors to the exchange of moisture in the Rivera Valley, Switzerland, and noticed that when the valley was resolved poorly, the cumulative daytime exchange was underestimated by a factor of three. Thus, the accuracy and resolution of the model is of great importance for resolving local flows in the valley and over the slopes. Resolutions less than 100 m are recommended for simulating thermally driven flows using LES (Cuxart, 2015).

LES modeling introduces an improvement upon subgrid parametrizations for eddies of all scales in Reynolds-Averaged Navier-Stokes simulations (Chow et al., 2013). LES resolve flow patterns by resolving larger scale eddies explicitly, and modeling smaller scale eddies containing smaller fractions of energy using turbulence

closure models. Advances in computational resources have made high-resolution LES more accessible, and there are a number of studies that have used a turbulent resolving LES mode in ideal cases (e.g., Arthur et al., 2018; Kirkil et al., 2012; Mirocha et al., 2014; Moeng et al., 2007; Muñoz-Esparza et al., 2016). However, due to computational costs real case runs over mountains are still rare (e.g., Chow et al., 2006; Gerber et al., 2018; Goger et al., 2022; Liu et al., 2020; Rai et al., 2017; Umek et al., 2021, 2022).

The development of nesting capabilities in NWP models has permitted application of new techniques to be investigated, such as transitioning from mesoscale to microscale regimes to obtain higher-fidelity turbulence information while preserving large scale forcing (Muñoz-Esparza et al., 2014; Wiersema et al., 2020). Results have shown some advantages for simulating turbulence at small scales while avoiding the gray zone (terra incognita regime, 1 km–100 m) (Chow et al., 2019; Wyngaard, 2004), and provide better predictions for surface variables and wind flows in complex terrain. To appropriately resolve slope and valley flows in mountains at high-resolution, LES are required along with high-resolution land use and topographic data. The Weather Research and Forecasting (WRF version 3.7.1) model (Skamarock et al., 2008), while intended for mesoscale atmospheric simulations, has a nesting feature, in addition to its LES capabilities, designed to run on massive parallel computers. It incorporates real world land use, topography, and regional scale meteorological data that are easily imported into the model.

The main objective of this experiment is to utilize LES to resolve and analyze differences in daytime thermally driven flows and near-surface atmospheric variables associated with two mountainous terrains with different valley volumes and surrounding orography during the snow-free season of a cold region, partly forested, high alpine environment. The study evaluates the effect of grid resolution, orography smoothing, and cloud parameterization resolution on model predictions to identify the best model configuration, which is then used to investigate the impact of topography on local flow features, air temperature and moisture, and cold-air pools.

2. Methodology

Simulations in this study, are focused on daytime convective conditions and predictions of thermally driven flow and meteorological parameters. The model performance for a global smoothing option to alleviate the numerical issues with steep terrain was compared to a local filtering algorithm, and a mesoscale one-dimensional planetary boundary layer (PBL) (turbulence is fully parametrized) simulation. The model domain and data used are described below.

2.1. Study Area and Data

The study area is located over the eastern side of the Canadian Rocky Mountains in the Kananaskis Valley, Alberta (Figures 1 and 2), which are characterized by a variety of steep slope angles and valleys. This experiment focused on two heavily instrumented mountain basins: Fortress Mountain Research Basin (FMRB) (50° 50′N, 115° 13′W) and Marmot Creek Research Basin (MCRB) (50° 57′N, 115° 09′W). FMRB (Figure 1c) contains wind scoured elevations of approximately 2,099–2,565 m. The alpine zone consists of two main ridges: Fortress and Canadian Ridges both oriented in SW-NE direction. Fortress Ridge has an elevation of about 2,300 m, adjacent to a shallow valley at an elevation of 2,000 m and orientation of 260°W, that is located in between Fortress and Canadian ridges. Canadian Ridge has an elevation of about 2,211 m, and average slope of ≈15° with some areas of ≈35° (Harder et al., 2016), while the mountain peaks exceed angles of 45°. Vegetation cover varies with elevation with shrubs and discontinuous coniferous forests at lower elevations (valley in between the ridges and slope sides) to alpine short grass (5–50 cm) at higher elevations (ridge tops), and bare alpine rocks at the steep slopes at highest altitudes. MCRB (Figure 1d) contains a greater variety of elevation ranges, from 1,600 m in the large U-shaped Kananaskis Valley located east of MCRB to 2,825 m at the summit of Mount Allan (Fang et al., 2013). Slope variation and vegetation in MCRB are similar to FMRB with the exception of more dense forests and milder topography at middle elevations, and an open, grassland valley floor to the east.

Simulations were verified using data collected by Sonic Detection And Ranging (SODAR) on 18 and 19 July 2016, from a flat surface on a ridge top at the east end of FMRB study area (Figure 1c) for remote measurements of the three-dimensional profiles of wind speed and direction in the lower portion of the ABL (i.e. <500 m). SODAR emits a number of acoustic pulse sweeps in each direction (north, east, south, west, and vertical) set to operate at a single frequency mode (1,650–2,750 Hz) (MFAS). Output resolution of vertical profiles were at 10 m
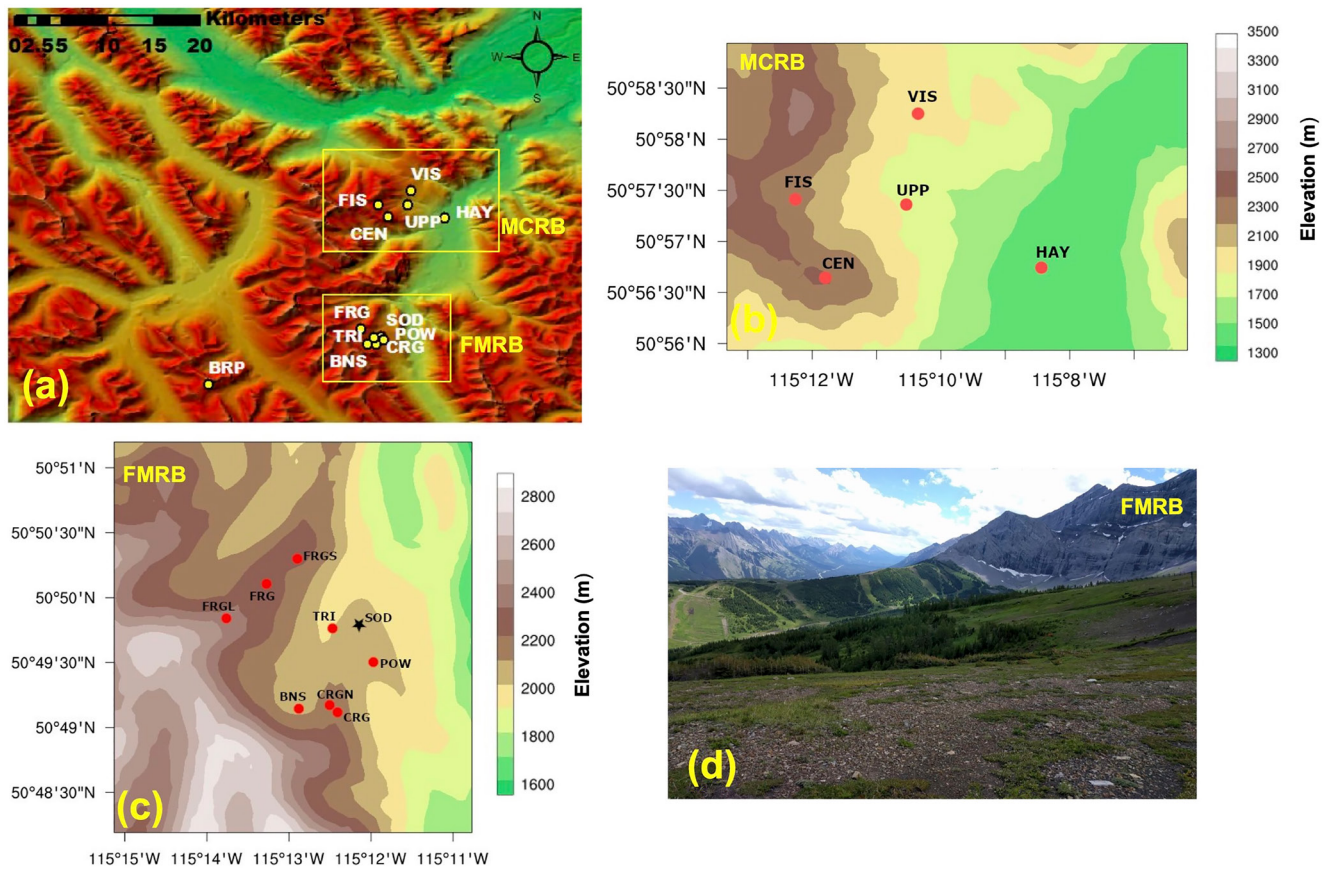
Figure 1. (a) Orography of the study area ($\Delta x = 90$ m) derived from the U.S. Geological Survey data set. The locations of meteorological stations at Marmot Creek Research Basin (MCRB), Fortress Mountain Research Basin (FMRB), and Burstall Pass Station (BRP) are marked by yellow circles; (b) The FMRB stations (locations indicated by points, and Sonic Detection And Ranging with a star), at 90 m grid spacing; (c) Similar to (b) but for MCRB area; (d) A picture of FMRB area from an eye view located near the FRG station, showing the valley area and a view of the Canadian ridge top (locations of CRG and CRGN stations).

intervals for heights 30–500 m AGL. Data was quality controlled and processed by APRUN software (Scintec, Germany), which determines wind speed and direction by examining the spectrum of backscattered wave for each cycle of SODAR sweeps.

Additional verification data were obtained from 13 meteorological stations (Figures 1b and 1c) located on ridge tops, valleys and a variety of aspects, slopes, and elevations at both FMRB and MCRB sites, and Burstall Pass located northwest of FMRB (Table 1). Meteorological stations include measurements of surface wind speed and direction (RM Young, Campbell Scientific, USA), incoming and outgoing longwave and shortwave radiative fluxes measured by CNR4 (Kipp and Zonen, Netherlands), and surface temperature and humidity (Rotronic sensors, Campbell Scientific, USA). Turbulent characteristics and fluxes were measured by a CSAT3 sonic anemometer (Campbell Scientific, USA) located at the north-west-facing slope station, Tripod (TRI), in FMRB. High frequency wind speed measurements were detrended and block averaged over 30 min intervals for flux estimates after applying a double rotation scheme (Kaimal & Finnigan, 1994) to align the coordinates with the mean wind.

2.2. Horizontal and Vertical Grid

In order to capture turbulent flows in high-resolution, the model was configured with 4 one-way nested domains (D1–D4), with a grid ratio of 3 at horizontal resolutions of 8.1, 2.7, and 0.9 km for the first three domains (Table 2). A grid refinement ratio of 10 was adjusted from D3 to D4 (Zhou & Chow, 2014) to avoid the gray zone associated with eddies at scales of a few hundred meters at mesoscale down to three-dimensional LES (Muñoz-Esparza et al., 2017; Wyngaard, 2004).

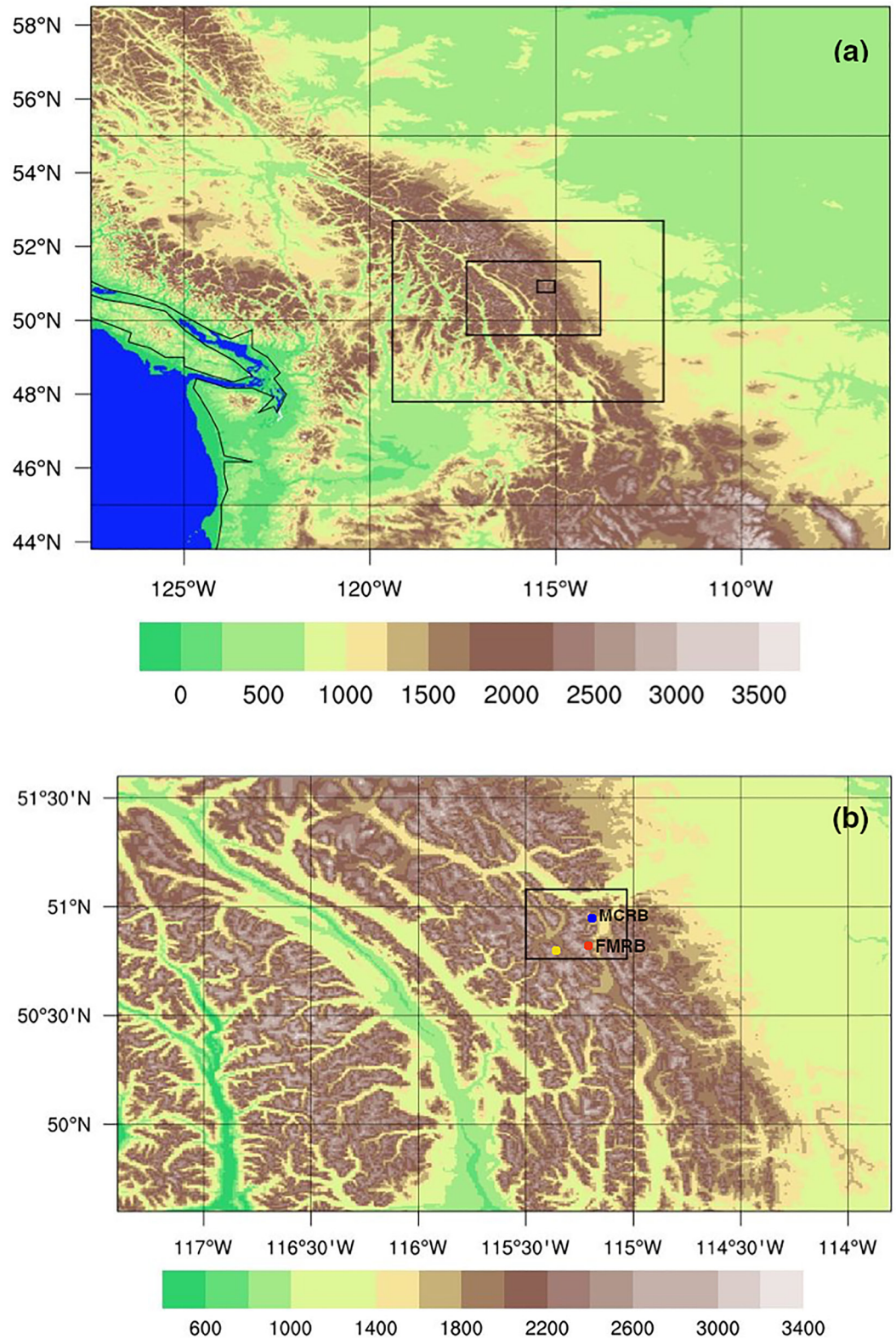**Figure 2.** (a) Mesoscale domains (D1–D3) at 8.1, 2.7, and 0.9 km grid spacing, respectively, and the innermost nested large-eddy simulation (LES) domain (D4) at resolution of 90 m; (b) D3 mesoscale domain at 0.9 km resolution containing LES domain (D4) at 90 m grid spacing. The blue (Marmot Creek Research Basin), red (Fortress Mountain Research Basin), and yellow (Burstall Pass) circles denote the location of study areas.

Table 1
List of Meteorological Stations With Coordinates and Elevation in Fortress Mountain Research Basin, Marmot Creek Research Basin, and Burstall Pass, Kananaskis Valley, Alberta, Canada, Shown in Figures 1b and 1c

Site	Name	Latitude (°N)	Longitude (°W)	Elevation (m)	Sensor height AGL (m)
FMRB stations					
TRI	Tripod (north-west-facing slope)	50.8278	−115.2077	2,060	2
BNS	Bonsai (valley floor)	50.8210	−115.2141	2,099	5
SOD	SODAR (ridge top)	50.8291	−115.2008	2,117	30–500
POW	Power Line (ridge top)	50.8260	−115.1983	2,136	5
CRGN	Canadian Ridge North (north-facing slope)	50.8217	−115.2066	2,205	6
CRG	Canadian Ridge (ridge top)	50.8214	−115.2063	2,211	3
FRGS	Fortress Ridge South (south-facing slope)	50.8382	−115.2157	2,310	5
FRG	Fortress Ridge (ridge top)	50.8257	115.19672	2,323	6
FRGL	Fortress Ledge (ridge top)	50.8300	−115.2286	2,565	3
MCRB stations					
HAY	Hay Meadows (valley floor)	50.9441	−115.1389	1,437	7
UPP	Upper Clearing (mid-level ridge top)	50.9565	−115.1754	1,845	3
VIS	Vista View (ridge top)	50.9709	−115.1722	1,956	3
FIS	Fisera Ridge (ridge top)	50.9568	−115.2044	2,325	2.6
CEN	Centennial (ridge top)	50.9447	−115.1937	2,819	2.5
BRP station					
BRP	Burstall Pass (ridge top)	50.7827	−115.3686	2,317	10

The larger parent domain (D1) covers an area $2,000 \times 2,000$ km^2, containing nests D2 and D3 down to nested domain D4, focusing on the study area covering a 36×36 km^2 domain (Figure 2). Limits of domain D2, D3, and D4 were specifically designed to avoid steep terrain to minimize model stability issues. Topography for mesoscale domains D1–D3 was set to the 30 arc-sec (1 km) U.S. Geological Survey (USGS) data sets available in WRF. Topography for LES domain D4 was extracted from a 3 arc-sec (90 m) USGS data set (Sertel et al., 2010), and the land cover for domain D4 was obtained from CanVec land use database at 50 m resolution.

A horizontal to vertical grid aspect ratio ($\Delta x/\Delta z$) between 3 and 5 is recommended in the LES domain to effectively resolve the vertical structure of the atmosphere near the surface and avoid distortion of the eddies (Chow et al., 2013). Vertical grids were distributed between ground level and 20 km (10 hPa) for a total of 80 levels stretched progressively from bottom to top of the model with a stretch coefficient of about 1.23 between the top levels. Below the first 1 km, 28 levels were used for all domains with $\Delta z_{\min} = 20$ m to allow for resolving turbulent structures within the boundary layer height over complex terrain, and to avoid overestimation of low level jet and contamination from overly diffusive structures (Muñoz-Esparza et al., 2017).

WRF uses a hydrostatic-pressure terrain-following vertical coordinate system, with stability issues arising from both the steepness of the terrain and grid aspect ratio (Daniels et al., 2016). It was determined that numerical instabilities due to the amplification of numerical errors caused by grid distortion near the surface along steep slopes results in vertical velocities violating the Courant-Friedrichs-Lewy (CFL) condition. To counteract numerical instability, some adjustments were applied. First, smoothing the terrain, increasing the time off-centering from WRF default of 0.1–1.0 that weights (forward in time) the vertically implicit acoustic-time-step terms in the model to dampen instabilities associated with sound waves propagating vertically in sloping model levels, and decreasing the time step were attempted. These solutions seemed to resolve the problem with numerical stability issues at the early start times in simulations, but continued to pose problems due to high lateral

Table 2
Large-Eddy Simulation Model Grid Configurations for Each Domain

Domain	Δx, Δy (m)	Grid points	Time step (s)
D1	8,100	202×202	1
D2	2,700	202×202	0.33
D3	900	271×241	0.11
D4	90	401×401	0.02

wind velocities over steep mountains in the simulations. To resolve this matter a sixth order diffusion option in WRF was applied to dampen the 2Δ waves, where Δ is grid spacing, for all variables in horizontal space (Knievel et al., 2007).

2.3. Turbulence and Physics Parameterizations

Vertical mixing (eddy transport of vertical fluxes) in WRF is parametrized using one-dimensional PBL schemes. Mesoscale domains D1–D3 make use of the YSU PBL scheme (Yonesi University) (non-local treatment of turbulent eddies using a critical Richardson number) (Hong et al., 2006) for vertical diffusion, and a two-dimensional Smagorinsky closure for horizontal eddy diffusivity (Smagorinsky, 1963). At the smallest model grid spacing in this study of 90 m for D4, LES aims to explicitly resolve the largest and most energetic eddies of the Inertial Subrange (Cuxart, 2015), with the assumption of cascade of energy to smaller sub-grid eddies, at which the turbulence is parametrized. In mountains, it is necessary to use fully three-dimensional turbulence schemes that represent observed small scale turbulent features occurring in a complex topography and relevant to resolving total kinetic energy (TKE) production in the valleys and slopes (Goger et al., 2018). In this study a full three-dimensional local 1.5 order prognostic TKE diffusion closure was deployed in the LES domain (D4) (Lilly, 1966, 1967).

Surface layer parametrization of Monin-Obukhov similarity theory (Monin & Obukhov, 1954) was set corresponding to specific PBL parametrization, and the LES surface layer was set to the revised surface layer scheme (Jiménez et al., 2012). The surface layer scheme provides information on friction velocities and exchange coefficients to WRF's Noah-MP land surface model (Niu et al., 2011) to calculate the turbulent fluxes. For cumulus parameterization, Kain-Fritsch (new Eta) (Kain, 2004) was used for the coarser domains, excluding the LES domain. Shortwave radiation was parametrized using the Dudhia scheme (Dudhia, 1989), which includes slope and shadowing effects on surface shortwave fluxes if corresponding namelist variables are activated. Longwave radiation was quantified using the rapid radiative transfer model (Mlawer et al., 1997). The longwave scheme does not include corrections arising from slope effects on incoming longwave radiation, which is a shortcoming in applying WRF in complex terrain.

2.4. Boundary Conditions and Mesoscale Model Initialization

To determine the best forcing conditions to be applied to the LES domain, sensitivity experiments were performed for the mesoscale domains (D1–D3). Three reanalysis data sets were used for the sensitivity tests: (a) the North American Regional Reanalysis (NARR) at 32 km resolution and with 30 vertical levels and a three-hour time step (Mesinger et al., 2006); (b) the Interim European Center for Medium-Range Weather Forecasts Reanalysis (ERA-Interim) at 77 km resolution, with 38 vertical levels and a six-hour time step (Dee et al., 2011); and (c) the Environment and Climate Change Canada GEM-based High Resolution Deterministic System forecast (HRDPS) at a resolution of 2.5 km, with 28 vertical levels and an hourly time step (Fillion et al., 2010). Five PBL schemes for vertical mixing in the mesoscale domains were also analyzed: (a) YSU; (b) Mellor-Yamada-Janjic (Janjić, 1994); (c) Mellor-Yamada-Nakanishi-Niino (MYNN) (Nakanishi & Niino, 2006); (d) Quasi Normal Scale Elimination (QNSE) (Sukoriansky et al., 2005); and (e) QNSE (a version of QNSE with non-local eddy diffusivity mass flux, EDMF). This combination of boundary data sets and PBL schemes generated 15 test cases in total to examine sensitivity. To evaluate the most accurate combination for initialization, hourly mean wind speed and wind direction for each of the vertical levels for both model 10 min output and SODAR 30 min data sets were calculated for the hours 7 a.m. to 9 p.m. Local Time. The mean root-mean-square error (RMSE) was then calculated for 27 vertical levels up to 300 m from ground level. RMSE is defined as

$$RMSE = \sqrt{\frac{1}{M}\sum_{j=1}^{M}\frac{1}{N}\sum_{i=1}^{N}(A_{ij} - B_{ij})^2} \tag{1}$$

where A_{ij} and B_{ij} are SODAR and simulation data, and M and N are the number of time steps and vertical grid points, respectively.

This analysis demonstrated that the combination of initial and boundary conditions from the HRDPS data set and all PBL schemes on average increased mean RMSE of wind speed by ≈0.6 m/s and wind direction by ≈2° with
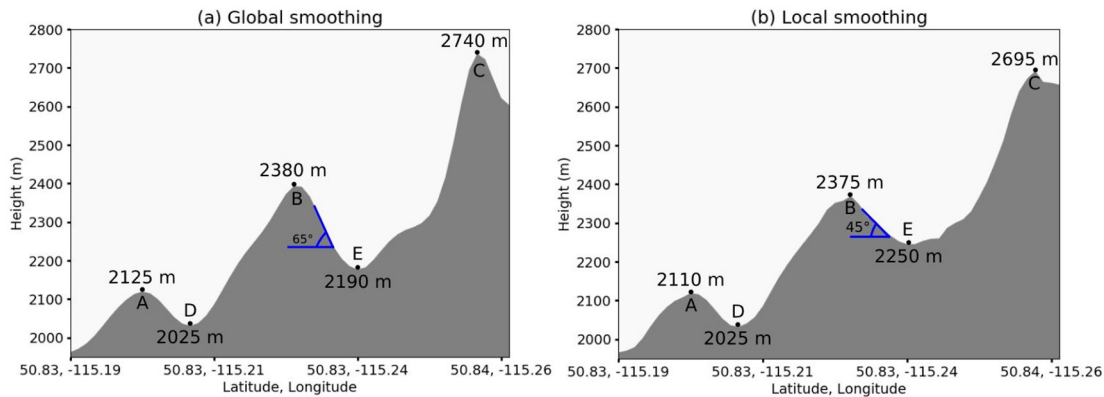
Figure 3. Example cross sections of global and local smoothing showing the differences in altitude of ridge tops, valleys, and a slope. Global filtering removes more valley features compared to local filtering, and local filtering smooths the steeper locations more than global filtering reducing the elevation of ridge tops.

respect to the other two reanalysis data sets. Combination of NARR data set and all PBL schemes resulted in a similar performance, with having reduced the errors by 10% for YSU PBL scheme. Combination of the NARR data set and QNSE PBL showed the largest error increased by 20%. Results for the two PBL schemes, YSU and MYNN, and in combination with the forcing data ERA-interim, showed the lowest mean RMSE for wind speed (≈ 0.45 m/s) and for wind direction ($\approx 11.5°$). Combination of ERA-interim with the YSU PBL was selected for the mesoscale simulations (D1–D3) for being more computationally efficient.

Soil moisture and temperature from the meteorological stations in FMRB and MCRB for 18 and 19 July were compared to all three meteorological data sets (i.e., ERA-Interim, NARR, HRDPS). The lowest bias belonged to ERA-interim with mean negative bias value of -0.07 m^3/m^3 for moisture and $+1°$ for temperature. Thus, ERA-Interim was chosen to initiate soil moisture and temperature at four soil model levels at ground level and 10, 30 and 100 cm below ground level.

2.5. Experimental Design

Domains (D1–D3) are mesoscale and use a PBL scheme for turbulence closure. Domain 4 uses an LES turbulence model to simulate the cascade of eddies from mesoscale to ABL convective scales, which are less than 100 m. WRF like most NWP models uses terrain-following coordinates, which can result in numerical errors in approximation of velocity gradients over steep slopes, causing numerical instabilities. To avoid this problem a global smoothing and local filtering approach was employed in which the local filtering only smoothed locations where the slope exceeds a given threshold.

The filters used in this study were: (a) global smoothing performed with a WRF smoother uniformly applied across all domains (D1–D4), hereafter referred to as LES with Global Filtering (LESGF) and (b) a local smoothing algorithm (Kosović, 2020) applied to D4. Global smoothing was applied to the coarser domains (D1–D3). This setup was referred to as LES with Local Filtering (LESLF). The first option filters the terrain significantly by applying 15 smoothing passes to stabilize simulations over steep terrain, which results in removing lower elevation and valley features, and generating unrealistic flows. To improve upon removing lower elevation orography, a local filtering algorithm was also tested that selectively filters terrain at slopes >45° to alleviate numerical divergence stability errors arising from steep terrain-following hydrostatic pressure (sigma) vertical coordinates of WRF (e.g., Arnold et al., 2012; Klemp et al., 2007). Figure 3 illustrates the differences in point-to-point comparisons of ridge tops, valleys, and a slope, in which local filtering smooths steep mountains more than global filtering (altitude differences in points A, B, and C, and slope angle), while global filtering removes more valley features, making the valleys deeper than reality (point E).

An additional LES with Local Filtering considers the impact of topographic shading and slope effects (LESLF_shade) on radiation by activating the namelist variables topo_shade and slope_rad in model setup. One more set up was also tested in which cumulus parametrization was activated only for the coarse parent domain, D1, in LESLF_shade_cloud simulations. The goal was to study the impact of model resolution on cloud fraction and radiation predictions when compared with LESLF simulations, which used cumulus parametrization for
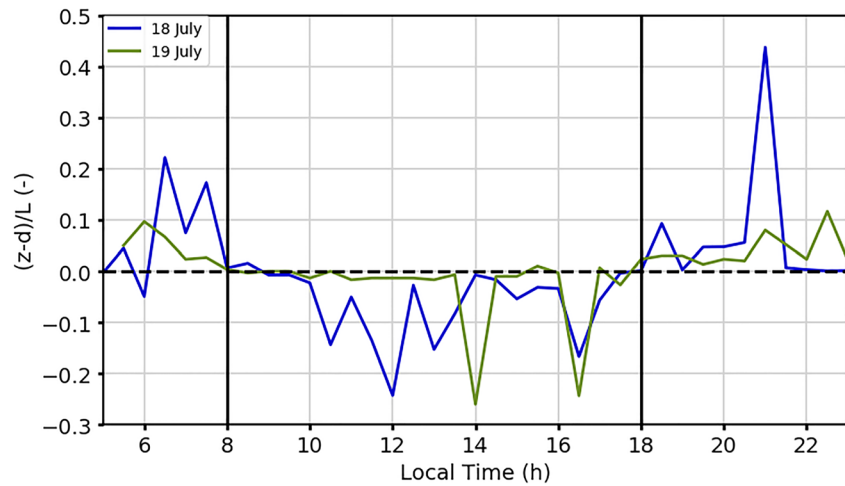
Figure 4. Time evolution of inverse Obukhov length for 5 a.m.–11 p.m. Local Time on 18 and 19 July derived from turbulent fluxes measured by sonic anemometer at 2 m above ground level at the TRI valley station.

all domains except D4. All LES configurations utilized the Cell Perturbation (CP) method (Muñoz-Esparza et al., 2015), which is most suitable for generating smaller turbulent eddies. The CP method provides better predictions of vertical profiles of turbulent eddies, by applying finite amplitude perturbations of potential temperature along LES inflow boundaries that lead to fully resolved turbulence spectrum within a reduced fetch.

A mesoscale experiment, named PBL, was performed using YSU PBL for turbulence closure to compare with LES experiments. Domains (D1–D4) were configured similar to LES experiments, except the resolution of domain D4 was set at 180 m. PBL experiments also used the topo wind namelist option that improves estimates of surface winds in mesoscale simulations and accounts for enhanced drag from sub grid topography in mountainous regions (Jiménez & Dudhia, 2012).

The choice of a suitable day for simulations was limited by the availability of sounding data on 18 and 19 July. Model forecasts are generally preferred for fair weather days with weak synoptic conditions (i.e., calm synoptic wind and clear skies) that represent the most unstable conditions, and thereby characterized by thermal flows. Typical wind speeds for upslope flows are between 1 and 5 m/s at a height of 20–200 m AGL (Zardi & Whiteman, 2013). On 18 July, wind speeds were generally lower and less than 5 m/s for most valley and ridge top stations, but forecasts were impacted by some periods of semi-cloudy skies. In comparison, 19 July had stronger mesoscale winds with wind gusts greater than 5 m/s reaching up to 12 m/s as observed at the ridge tops in FMRB and MCRB study areas. The stronger wind gusts can overwhelm more subtle thermally driven local flows.

The suitability of the chosen days for model simulations was narrowed down further by investigating the evolution of inverse Obukhov length (L) (Figure 4) calculated from the observed turbulent fluxes at the valley station (TRI) scaled with sonic anemometer height (z) and corrected with vegetation height (H) (Hogstrom, 1990), $(z - d)/L$, where $d = 0.75$ H ≈ 40 cm is the displacement height. After sunrise ($\approx$8 a.m. Local Time at this location), the ABL switched from stable ($(z - d)/L > 0$) to unstable conditions ($(z - d)/L < 0$) for both 18 and 19 July. $-0.5 < (z - d)/L < 0$ during unstable hours suggests that shear production was the dominant source for turbulent production (Wyngaard, 1973). Late afternoon boundary layer on both days resumed nighttime stable stratification ($(z - d)/L > 0$) after 6 p.m. 18 July showed enhanced amplitude in shear and convective turbulent instabilities (10 a.m.–6 p.m.) that helps to drive valley and slope flows. To better evaluate model performance in thermally driven flows, the rest of this paper is focused only on the 18 July forecasts.

All simulations for domains D1–D3 were initialized at 06:00 UTC on 18 July to permit 6 hr of spinup period. Initial and boundary conditions for D4 were initialized from the output of D3 at 12:00 UTC on 18 July to run concurrently after spinup period. Experiments were run for 16 hr physical time since the main focus of this study was on daytime flows (5 a.m.–9 p.m. Local Time). Frequent forecasting outputs were generated at time intervals of 10 min for the D4 domain for both LES and PBL simulations. Time series of some surface variables and vertical profiles of wind components, temperature, and water vapor were also output at every model time step at

each meteorological station location. Since the instantaneous model output is not a full representation of the time dependent processes in the LES domain, the time series output was averaged for each 15 min interval to account for an ensemble of turbulent fluctuations. This makes it more comparable with measured surface variables averaged over the same period of time.

The setup above was computationally costly, which resulted in simulations requiring 12 hr CPU time for every 2.3 hr of physical time. This required 20 (720 cores) nodes/cores for the 4-domain simulations on the Cheyenne cluster at the NCAR supercomputer research facility.

3. Results and Discussions

The impact of LES with local filtering method, with and without topographic shading (LESLF_shade and LESLF, respectively), along with the results from simulations of local filtering LES with lower resolution cloud parametrization (LESLF_shade_cloud), global filtering LES (LESGF), and mesoscale simulations (PBL) on daytime air flow (5 a.m.–9 p.m. Local Time) for near-surface forecasts are compared to observations.

3.1. Time Series and Diurnal Cycle

The impact of topographic dependent vegetation, cloud and mountain shading, and elevation differences on radiation, slope and valley winds in complex terrain are investigated using surface time series at four different sites. The diurnal evolution of radiation, surface wind speed and direction at valley and ridge top stations are presented as follows: Bonsai (BNS) and Power Line (POW) stations in FMRB, and Hay Meadow (HAY) and Fisera Ridge (FIS) stations in MCRB (Figure 1 and Table 1). The valley station (BNS) is located on the valley bottom, while the ridge top station (POW) is on a gentle slope (<10°) rising to the northeast. BNS and POW are considered "sheltered" sites as they are 15 m diameter clearings surrounded by coniferous forests, in addition to mountain ridges providing topographic shading at the valley site. In MCRB, the valley station (HAY) is located on the valley bottom, while the ridge top station (FIS) is on a level ground, with a ridge located to the west that slopes upward to the west. Land cover at HAY and FIS consists of sparse grass and bare ground located in a well exposed wide valley and high ridge top, respectively and so are considered "open." The vertical profiles and time series of wind speed and direction are also evaluated against SODAR for the simulated day, 18 July.

3.1.1. Radiation

Figure 5 illustrates simulated and observed surface net radiation and biases for each set of model configurations and observations. In mountainous areas, the surface radiation budget is modified by topographic shading and cloud cover (Zardi & Whiteman, 2013). All simulations showed some degree of overprediction of radiation in the early hours at all locations, with the highest overprediction seen at the sheltered ridge top station (POW) in FMRB. In the afternoon, at BNS, LESLF_shade_cloud, and PBL overestimated radiation, while the rest of the simulations underestimated radiation by about ±400 W/m². Similarly, at POW and open valley station (HAY), all simulations underestimated radiation, but LESLF_shade_cloud closely followed observations at both locations. At the open ridge top (FIS), all the simulations except LESLF_shade overpredicted radiation for various durations.

The discrepancies between the model predictions and observations of radiative fluxes especially early in the day are attributed to several factors, including orographic smoothing and the subsequent modulations in shortwave fluxes. Differences in elevation between LES results and reality may have contributed to the inconsistencies in predictions of radiative fluxes, which varies from none at the mid-altitude station, Upper Clearing (UPP), in MCRB to about 423 m at the ridge top station, Centennial (CEN), in MCRB.

The effect of topographic shading during a day with cloudy periods is difficult to ascertain from the current results. That is, in some instances LESLF_shade followed the observed fluxes better than LESLF, and vice versa. The sudden rise in the observed net radiation before sunrise in the valley sites (BNS and HAY) indicated shadowing by the surrounding mountains. At POW, sunrise occurs approximately 2 hours later than at the sheltered valley station (BNS) in the morning. The early morning lag in radiative flux measurements persisted over the summer months at POW, indicating that topographic shading by the slope rising to the northeast is responsible for the sunrise lag at this location. Simulations failed to follow observations possibly due to misrepresentation of the orography in the simulations. Additionally, short-lived cumuli (i.e., ground
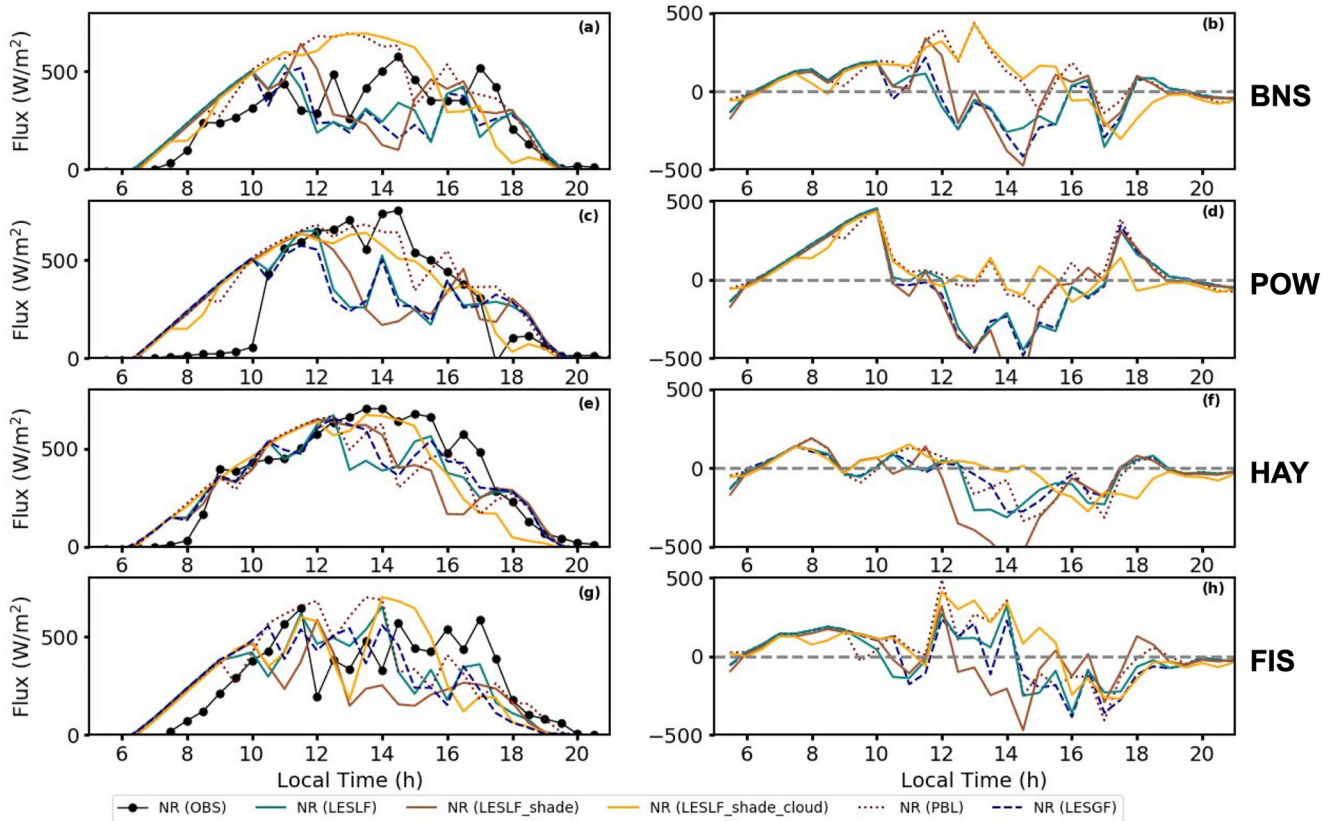
Figure 5. Net radiation fluxes (net shortwave and longwave radiation) (left), and biases between each model configurations and observations (right) at the sheltered valley (BNS, (a, b)), sheltered ridge top (POW, (c, d)), open valley (HAY, (e, f)), and open ridge top (FIS, (g, h)) stations.

level up to 700 hPa) reduce the amount of shortwave flux received by the surface, and modify heat and moisture fluxes. Hence, their correct representation in high-resolution simulations is crucial for accurate predictions of radiation, and local wind flows in complex terrain. Nonetheless, LESLF_shade_cloud model with the lower resolution in cloud parametrization (activated only in the first coarse domain D1), overall is the most successful in predictions of radiative fluxes. The analysis confirms that nested high-resolution runs can be affected by the incorrect input for convection processes from the coarser domains (i.e., gray zone), suggested by other studies (e.g., Jeworrek et al., 2019), resulting in incorrect predictions of clouds in the finer resolution LES domain.

3.1.2. Potential Temperature, Wind Speed, and Direction

In Figure 6a simulated vertical profiles of potential temperature at three different timestamps chosen to correspond with SODAR observations are compared to illustrate the evolution of the ABL during daytime hours. At 9 a.m. Local Time, simulations showed a developing mixed layer near the ground in the potential temperature profile at approximately 100 m above ground. Above this mixed layer the atmosphere is stably stratified. In the afternoon, the atmosphere revealed a well-mixed layer, indicating a convective ABL due to warming up of the surface layer. In the late afternoon, a stable ABL seemed to be establishing, evident in the corresponding potential temperature profile.

Figures 6b–6e compare simulated wind speed and direction with SODAR profiles for 30–500 m AGL. For the sake of consistency, wind speed profiles are made using the output of an integrated data collection of 8 min in each cycle of SODAR sweeps, and time-averaged fluctuations of model output for the same time interval of SODAR cycle. SODAR profiles suffered from incompleteness and low measured heights in some measurement cycles (i.e., <300 m) possibly caused by strong low level winds or lack of turbulence and temperature gradients, which often happen during morning and evening transitions. The progression of vertical profiles have been arranged to show examples of the flow at the SODAR location from afternoon of 18 July, when sounding measurements reached a height of more than 400 m AGL for better evaluation.
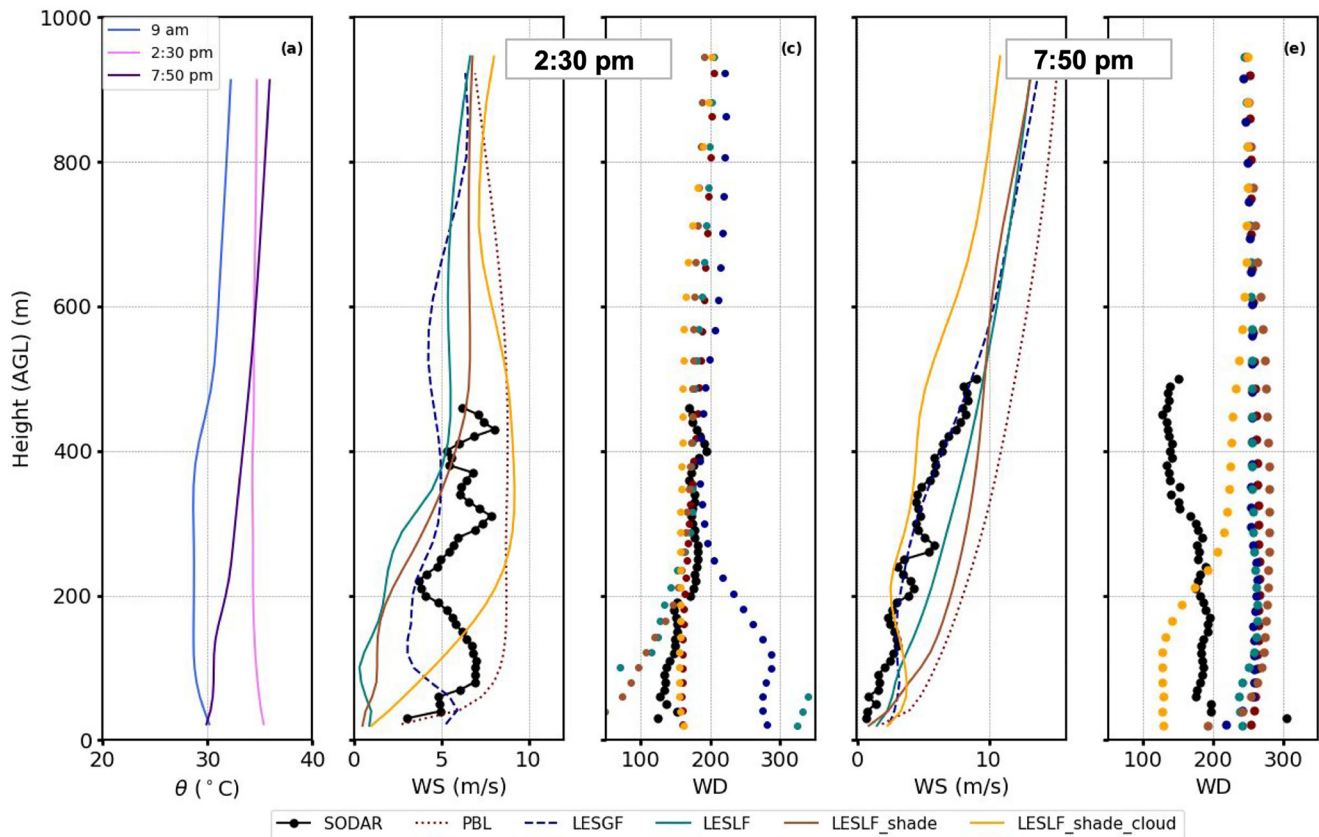
Figure 6. (a) Vertical profiles of potential temperature showing the evolution of atmospheric boundary layer at 9 a.m., 2:30 p.m., and 7:50 p.m. Local Time (LT). (b–e) The 2:30 p.m. and 7:50 p.m. LT (18 July) vertical profiles of Sonic Detection And Ranging, compared with LESLF_shade_cloud, LESLF_shade, LES with Local Filtering, LES with Global Filtering, and planetary boundary layer Weather Research and Forecasting simulations of wind speed and wind direction.

At 2:30 p.m. Local Time, PBL and LESLF_shade_cloud predicted the flow direction most successfully, but wind speed was either underestimated or overestimated by all simulations at various heights above ground, expect PBL which was most successful in predicting the low-level jet at this time. The late afternoon (7:50 p.m. Local Time) wind profile observation from SODAR revealed that near-ground winds remained at approximately 180°–200°. None of the simulations were quite successful in predicting wind direction, and deviations are <80° at below 200 m. LESGF was the most successful in predicting wind speed at this time except near the ground, and LESLF_shade_cloud followed observations closely in between 50 and ≈400 m above ground.

Time series evolution of wind speed and wind direction illustrates model performance with different configurations at 40 m AGL (Figure 7). Suitable SODAR observations were available for only a portion of 18 July. The simulated time series of wind speed for the LES results showed a progressive growth in amplitude of wind speed fluctuations from morning to the afternoon. This is consistent with the growth of a mixed boundary layer (Figure 6a), which is corroborated by SODAR observations. PBL model also showed growth in amplitude of fluctuations in horizontal wind speed from morning to the afternoon, but displayed higher RMSE than LESLF simulations (Table 3). LESLF_shade_cloud presented the best performance (Figure 7b), and the lowest RMSE for wind direction compared to the rest of simulations (Table 3).

To study the thermally driven flows at each of the station locations, model output for wind speed and wind direction at 10 m AGL were compared to station data collected at various instrument heights (2–10 m AGL). To avoid discrepancy between differing model and sensor height measurements, model forecasts were corrected to the sensor height using a logarithmic wind profile under the assumption of a neutrally stratified atmosphere. Due to complexity of terrain at these sites, wind speed and direction vary in different patterns for each of the station locations.
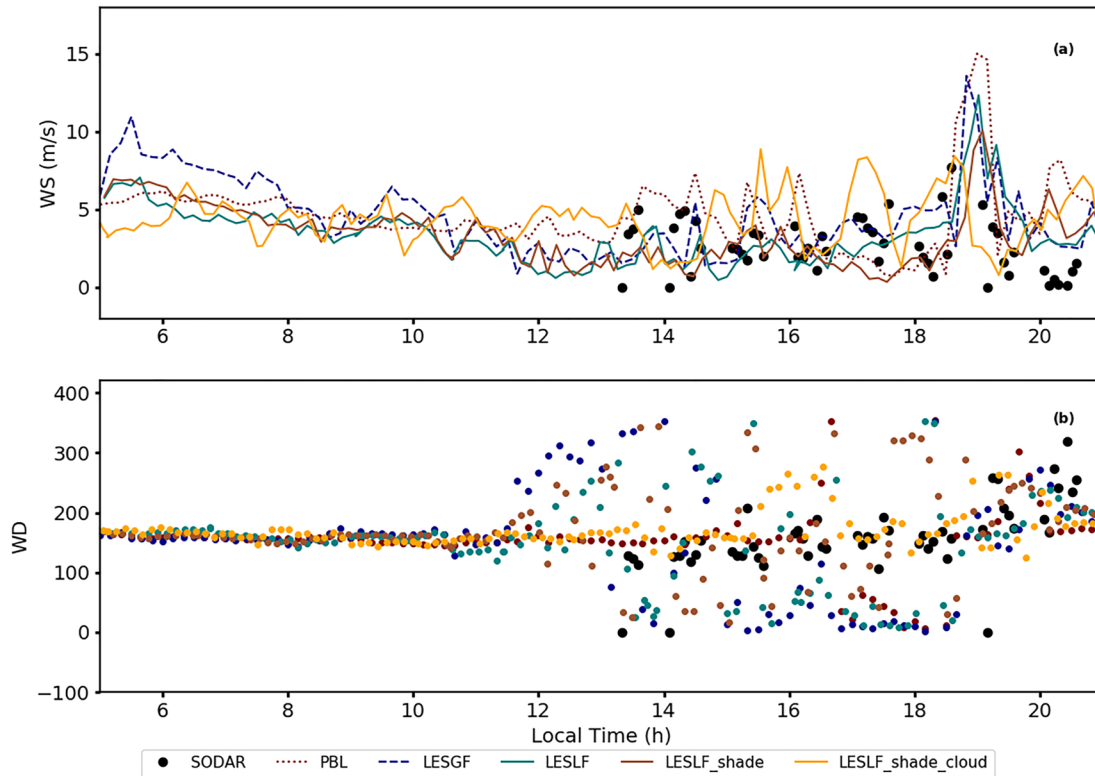
Figure 7. Time series evolution of wind speed and direction at 40 m above ground level on 18 July (a, b).

At the BNS sheltered valley station in FMRB (Figure 8), wind speed remained consistently low, below 2 m/s, after sunrise at 8 a.m., with a slight increase in the afternoon. The dominant wind was down-valley ($\approx 150°$–$250°$) before noon, and started to turn into an up-valley flow after 11:30 a.m. The surface flow at BNS switched between up-valley ($300°$–$350°$ and $0°$–$50°$) and down-valley the rest of the day, until after sunset at 7 p.m. when it eventually turned back to down-valley. LESLF simulations showed improvement in predicting wind speed (RMSE = 0.6 m/s), when compared to PBL (RMSE = 0.9 m/s) and LESGF (RMSE = 1.0 m/s). All simulations had difficulty with wind direction predictions in some instances throughout the day, but all simulations except LESLF_shade_cloud and PBL predicted the transition from down-valley to up-valley more successfully. The difference in wind direction pattern between the model and observations throughout the day might suggest that in reality, wind direction followed a complex pattern because of sub-canopy turbulence and the impact of surrounding topography. In sheltered sites, wind direction can be affected by turbulent fluctuations caused by under-canopy turbulence (Conway et al., 2018). Sub-canopy turbulence and flow reversals are characteristics that can cause frequent and sudden changes in wind direction. It is noted that the model does not represent the effect of shading by vegetation on surface parameters. There is also high variability in surface vegetation heights in surrounding terrains, and a wide range in aerodynamic roughness length ($z_0 = 0.06$–1.1 m) that the current model resolution does not capture.

At the ridge top sheltered site in FMRB, POW (southeast-facing slope) (Figure 8), wind speed was very low in the very early hours before sunrise, but increased after 7 a.m. and changed direction from the very weak drainage flow, possibly dampened by the surrounding vegetation ($\approx 300°$–$350°$ and $0°$–$50°$), to upslope ($\approx 200°$) during daylight hours. This persisted until about 7 p.m. before returning to downslope again at sunset. All simulations provided similar predictions for wind speed and direction, except in the early hours during model spin up, and stayed within the upslope range ($\approx 100°$–$200°$) after the morning transition. LESLF_shade_cloud presented the lowest RMSE (RMSE = 0.9 m/s) for wind speed and (RMSE = 54.5°)

Table 3
Root-Mean-Square Errors (RMSE) for Wind Speed (m/s), and Wind Direction (°)

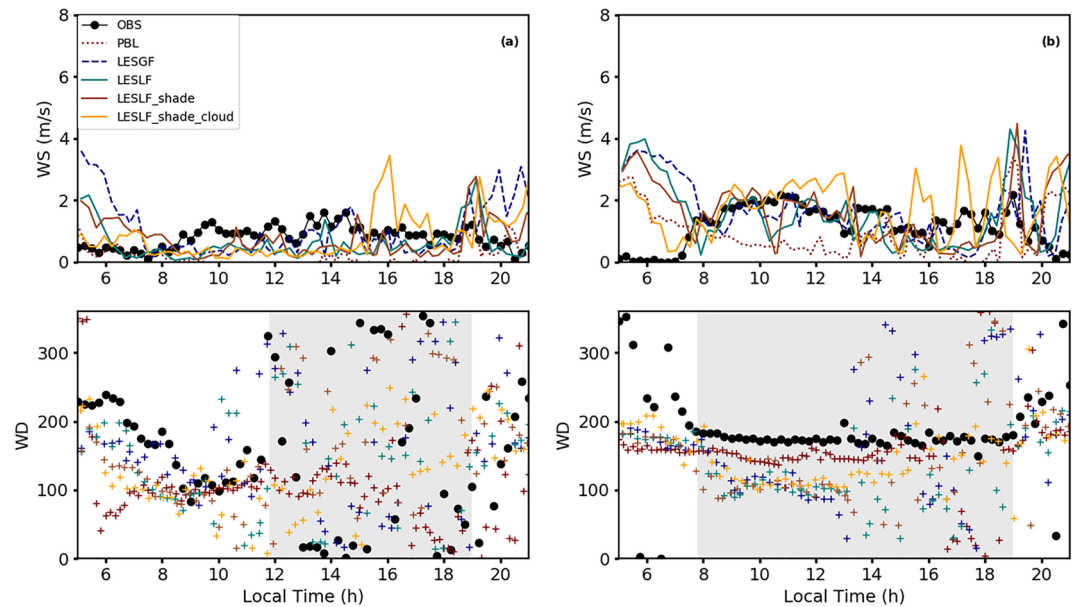| Model	WS	WD
LESLF_shade_cloud	3.3	72
LESLF_shade	2.9	104
LESLF	3.2	109
LESGF	3.3	144
PBL	4	90

Figure 8. Surface wind speed and direction at the sheltered valley (BNS, (a)) and ridge top (POW, (b)) stations located in Fortress Mountain Research Basin. The shaded areas highlight the periods in which the flow was essentially up-valley at BNS, and upslope at POW.

direction, and showed less fluctuations in the afternoon predictions of wind direction compared to the other simulations. The frequency of fluctuating wind direction could be due to convective patterns related to surface fluxes and radiative transfer (i.e., cloud shading) in each of the simulations.

At the open valley site (HAY), simulations predicted the onset of up-valley wind and transition from down-valley ($\approx250°$–$320°$) to up-valley ($\approx100°$–$200°$) relatively close to observations (Figure 9). Observed wind direction showed that wind was up-valley in the afternoon before transitioning back to down-valley after 6 p.m., while
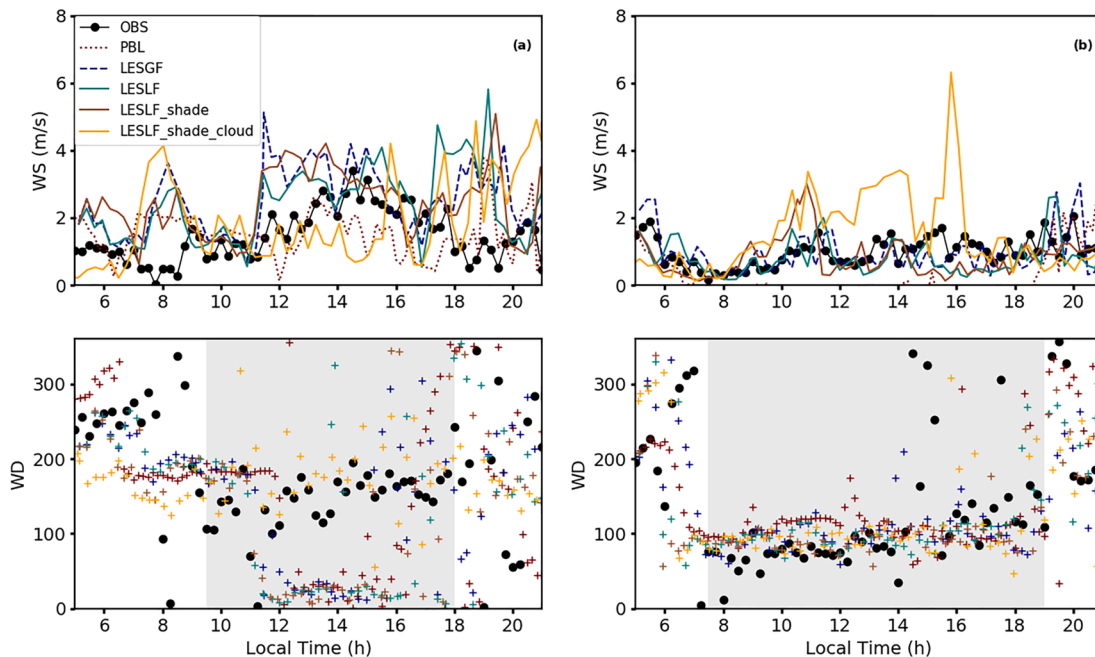

Figure 9. Surface wind speed and direction at the open valley (HAY, (a)) and ridge top (FIS, (b)) stations located at Marmot Creek Research Basin. The shaded areas highlight the periods in which the flow was up-valley at HAY, and upslope at FIS.
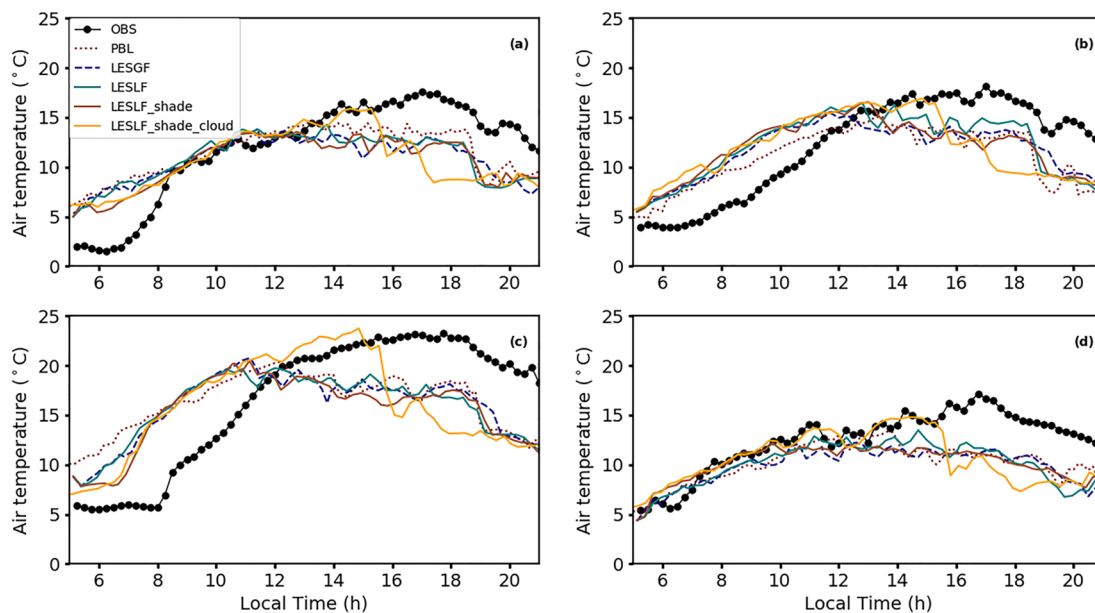
Figure 10. 2-m air temperature at the sheltered valley (BNS, (a)), sheltered ridge top (POW, (b)), open valley (HAY, (c)), and open ridge top (FIS, (d)).

all simulations except LESLF_shade_cloud continued to predict a down-valley flow into the afternoon hours. Since this site was not shaded by the surrounding mountains during mid-day hours, the better agreement between LESLF_shade_cloud and observations seems to be related to better predictions of net radiation at this location (Figure 5).

Higher elevation ridge tops are generally exposed to solar radiation earlier than valley bottoms, and upslope flows are expected to form before up-valley flows (Lehner & Rotach, 2018; Serafin et al., 2018). The timing of the onset of upslope flow toward west over the open ridge top (FIS) agreed with an earlier formation of upslope wind (≈7 a.m.) compared to the onset of the up-valley flow (≈9 a.m.) at the HAY station. This was similarly observed at the BNS valley station when the up-valley flow developed with a delay compared to the upslope flow at the POW station. The drainage flow at FIS is complex, with winds flowing mainly toward the east, but sometimes toward the south, influenced by the higher elevations and mountain peaks to the west and north. LESLF_shade_cloud showed the lowest RMSE in wind direction (RMSE = 77°) at the FIS station. LES results overestimated wind speed at the HAY station, and PBL had the lowest RMSE at this location (RMSE = 0.9 m/s). All simulations presented good agreement with the observed wind speed at the FIS station, except LESLF_shade_cloud that overestimated wind speed at some instances.

3.1.3. Air Temperature

The surface evolution of 2 m air temperature at the four sites (BNS, POW, HAY, and FIS) is shown in Figure 10. The simulations overestimated temperature in the morning at the valley sites (HAY and BNS) with biases of 6 and 4°C, respectively, right after sunrise. The overestimation of morning temperature is related to the model's under-representation of cold-air pools in mountain valleys (e.g., Pagès et al., 2017; Zhang et al., 2013), and over prediction of radiative fluxes (Figure 5). Vionnet et al. (2015) reported the impact of valley cold-air pools on temperature biases during wintertime at valley and high-altitude stations in the Canadian Rockies using the GEM meteorological model. Their findings showed that the diurnal cycle at the HAY station was impacted by cold-air pool formation at night and early morning, but cold-air pools did not impact another station, Vista View (VIS), in MCRB located on a valley side at mid-elevations. Similar to Vionnet et al. (2015), this study finds that the warm bias was lower at higher elevations (BNS, POW and FIS) at 8 a.m. with biases less than 2°C, with the POW warm bias persisting longer in the morning compared to all other locations, likely related to topographic shading similar to the lag in sunrise at this location.

As the valley nocturnal temperature inversion broke up with daytime heating, warm biases were reduced with very close performance for simulations but better predictions from LESLF_shade_cloud. When BNS and HAY

Table 4

Bias and Root-Mean-Square Errors for Wind Speed (m/s) and Wind Direction (°) for Simulations Compared With Observations at All Meteorological Stations in Both Fortress Mountain Research Basin and Marmot Creek Research Basin Sites (See Table 1) for the Simulations Tested

Model	Met station	WS bias	WD bias	WS RMSE	WD RMSE
LESLF_shade_cloud	All	0.7	5.7	1.6	72
LESLF_shade_cloud	Fortress Mountain	1.2	6.3	1.9	72.5
LESLF_shade_cloud	Marmot Creek	−0.1	−3.7	1.3	73.8
LESLF_shade	All	0.2	−4.6	1.4	74
LESLF_shade	Fortress Mountain	−0.3	−26	1.1	75
LESLF_shade	Marmot Creek	0.4	2.8	1.7	74.6
LESLF	All	0.1	−10.8	1.3	72
LESLF	Fortress Mountain	0.3	−10.3	1.5	72.6
LESLF	Marmot Creek	−0.3	−23.3	1.1	72.8
LESGF	All	0.4	−3.7	1.3	77
LESGF	Fortress Mountain	0.6	5	1.6	78
LESGF	Marmot Creek	0.0	−26.3	1.0	78
PBL	All	−0.5	−2.8	1.2	75.5
PBL	Fortress Mountain	−0.3	−6.9	1.2	76.7
PBL	Marmot Creek	−0.9	−10.0	1.3	73.6

Note. For comparison site specific statistics at only FMRB and MCRB stations are also reported.

Table 5

Bias and Root-Mean-Square Errors for Air Temperature (K) and Specific Humidity (g/kg) for Simulations Compared With Observations in Fortress Mountain Research Basin and Marmot Creek Research Basin Sites

Model	Met station	T bias	Q bias	T RMSE	Q RMSE
LESLF_shade_cloud	All	−0.6	2.6	4.3	3.5
LESLF_shade_cloud	Fortress Mountain	−0.4	2.4	4.9	3.8
LESLF_shade_cloud	Marmot Creek	−0.8	2.6	3.9	2.8
LESLF_shade	All	−0.8	3.4	4.6	4.4
LESLF_shade	Fortress Mountain	−1.2	3.9	4.0	4.3
LESLF_shade	Marmot Creek	−0.4	3.0	5.2	4.5
LESLF	All	−0.6	3.5	4.2	4.6
LESLF	Fortress Mountain	−0.2	3.2	4.8	4.7
LESLF	Marmot Creek	−1.1	3.9	3.6	4.3
LESGF	All	−0.9	3.4	4.4	4.4
LESGF	Fortress Mountain	−0.5	3.0	4.9	4.6
LESGF	Marmot Creek	−1.4	3.7	3.8	4.1
PBL	All	−0.9	3.5	4.1	4.4
PBL	Fortress Mountain	−0.5	3.1	4.6	4.1
PBL	Marmot Creek	−1.1	4.0	3.5	4.9

Note. For comparison site specific statistics at only FMRB and MCRB stations are also reported.

observed temperature evolution an hour after sunrise (9 a.m. Local Time) are compared, the removal of cold-air pool due to daytime heating happened slightly earlier in the FMRB valley than in the valley of MCRB, although the narrower FMRB valley is sheltered more by the surrounding topography (Figure 1c). The persistence of cold-air pools in HAY located in the deep and wide Kananaskis Valley (Figure 1b) can be related to an elevated inversion layer, and it will be discussed further in Section 3.3. Continuing into the afternoon, all simulations showed a cold bias at all four locations, regardless of differences in elevation or net radiation biases (Figure 5). Model resolution does not seem to have an impact on predictions, and both LES results and PBL showed similar performance for the later afternoon temperature predictions. The rise in maximum observed daytime air temperature of the two sheltered sites, POW and BNS, with smaller elevation differences (≈40 m) followed a closer diurnal trend, than HAY and FIS with greater altitude (≈900 m) differences.

3.2. Bias and Error Analysis

Table 4 summarizes the bias and RMSE error statistics at all stations for surface wind speed, and wind direction in FMRB and MCRB. Biases are calculated using,

$$bias = \frac{1}{N} \sum_{i=1}^{N} (A_i - B_i) \qquad (2)$$

where A_i is simulation and B_i is observed data, and N is the time step. Overall, wind speed bias between simulated data and observations for all stations at both sites in this study was lowest for LESLF without shading, but RMSE error was slightly lower for PBL. Taking both bias and RMSE error for wind direction into account, LESLF_shade_cloud performed better than the rest of the simulations. If only FMRB sites are considered, LESLF_shade presented the lowest RMSE for wind speed between all the simulations tested, and LESLF_shade_cloud and LESLF presented close proximity errors for wind direction.

Table 5 summarizes the bias and RMSE error statistics at all stations for surface air temperature and specific humidity in FMRB and MCRB. LESLF_ shade showed the least agreement with observations for RMSE error in air temperature between the tested simulations, and LESLF_shade_cloud provided lowest RMSE error for surface specific humidity. If RMSE errors and biases for all surface parameters at all station are taken into account, and SODAR evaluations are considered, LESLF_shade_cloud is eventually chosen as the winning model.

3.3. Impact of Topography on Near-Surface Boundary Layer Characteristics

When dealing with very complex terrain, such as FMRB and MCRB mountainous areas, the surrounding topography and geometry of the valley can impact near-surface thermal flows particularly in the valleys. Helgason and Pomeroy (2012) discovered frequent wind gusts transported turbulent energy from higher elevation complex terrain surrounding the Kananaskis River Valley to the HAY valley station, which affected the rate of energy transfer at the surface. Large-scale topographical disturbances were found to contribute to turbulent fluxes in the valley area.
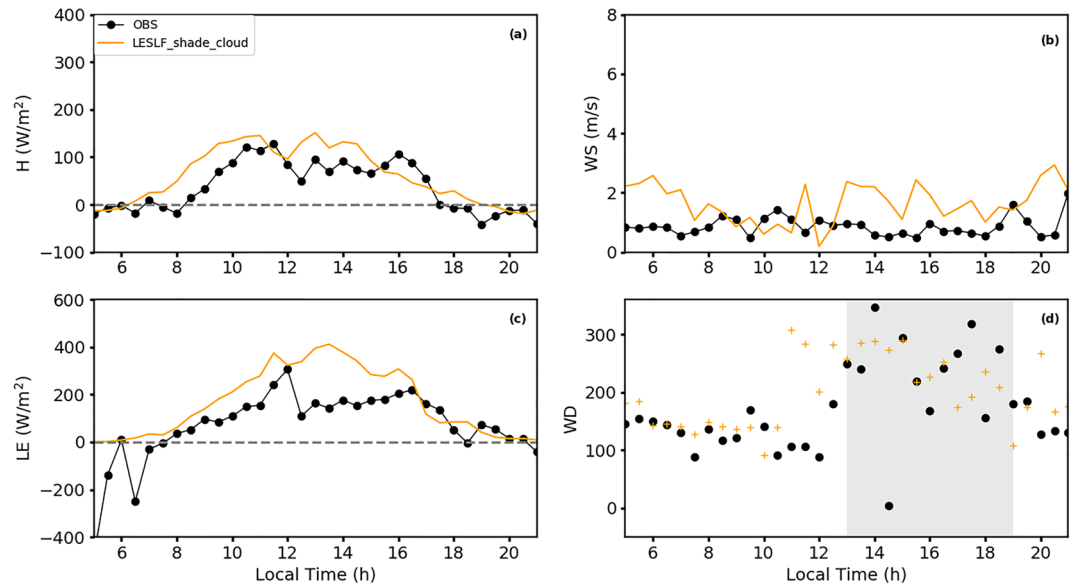
Figure 11. Surface sensible heat and latent heat fluxes (a, c), wind speed (b), and wind direction (d) at the north-west-facing slope station (TRI). The shaded area highlights the flow when it was up-valley.

To investigate the effect of surrounding topography on local winds, the best performing model, LESLF_ shade_cloud predictions were compared against observations at a different location in the FMRB valley. The north-west-facing slope station, TRI (Figure 1), equipped with eddy covariance measurements, is located ≈300 m away from BNS. The TRI station is on a gentle slope near the valley bottom, ≈30 m higher in elevation, and is affected by the valley flows. The simulated sensible and latent heat fluxes, and wind speed and direction were compared against observations in Figure 11. Model provided reasonable predictions of surface fluxes, but the simulated wind direction had difficulty following observations when the wind switched between up-valley and down-valley in the afternoon hours similar to the BNS station.

Figure 12 depicts snap shots of complex flows in the FMRB and MCRB study areas, where the red dots represent the locations of valley stations, BNS in FMRB, and HAY in MCRB. The simulated surface wind at 10 m AGL at the BNS valley station at FMRB revealed the presence of a down-valley flow in the morning and upslope flows toward the higher elevations (Figure 12a). At MCRB, the down-valley flow near the HAY station seems to be impacted by the stronger winds blowing from the south end of the valley (Figure 12b), and there is presence of upslope flows toward the higher elevations.

At both the mountain valleys, the simulated afternoon up-valley flows are disrupted by the cross-valley winds or short-lived wind gusts, frequently observed at the higher elevations in the study areas, blowing from the mountain ridges toward the lower elevations (Figures 12c and 12d). This further illustrates the complex interactions of mesoscale and thermally driven flows within mountain valleys.

The general topography and orientation of FMRB and MCRB could contribute to differences in up-valley wind strength. Valley geometry has an impact on valley wind formation and strength. Ideal simulations by Wagner et al. (2015) have shown that up-valley winds are weaker for wider and shallower valleys, while deeper valleys are conducive to an elevated inversion layer and stronger up-valley flows. The Kananaskis Valley at MCRB is wide, runs north-south and connects to a larger valley (Bow Valley), as compared to FMRB area that has a narrower valley with more compact side walls surrounding it and more of a south-west-north-east orientation. The depth differences between a valley bottom and the tallest ridge top with a meteorological station differ substantially, being 1,400 m in MCRB and 500 m in FMRB. The breakup of nocturnal inversion, and transition from a down-valley to up-valley flow depends on the warming of convective boundary layer by heated surface layer. The subsidence of warmer air substituting cooler air in the valley compensating for upslope flow is equally important, but the process can be facilitated by valley geometry (Zardi & Whiteman, 2013).
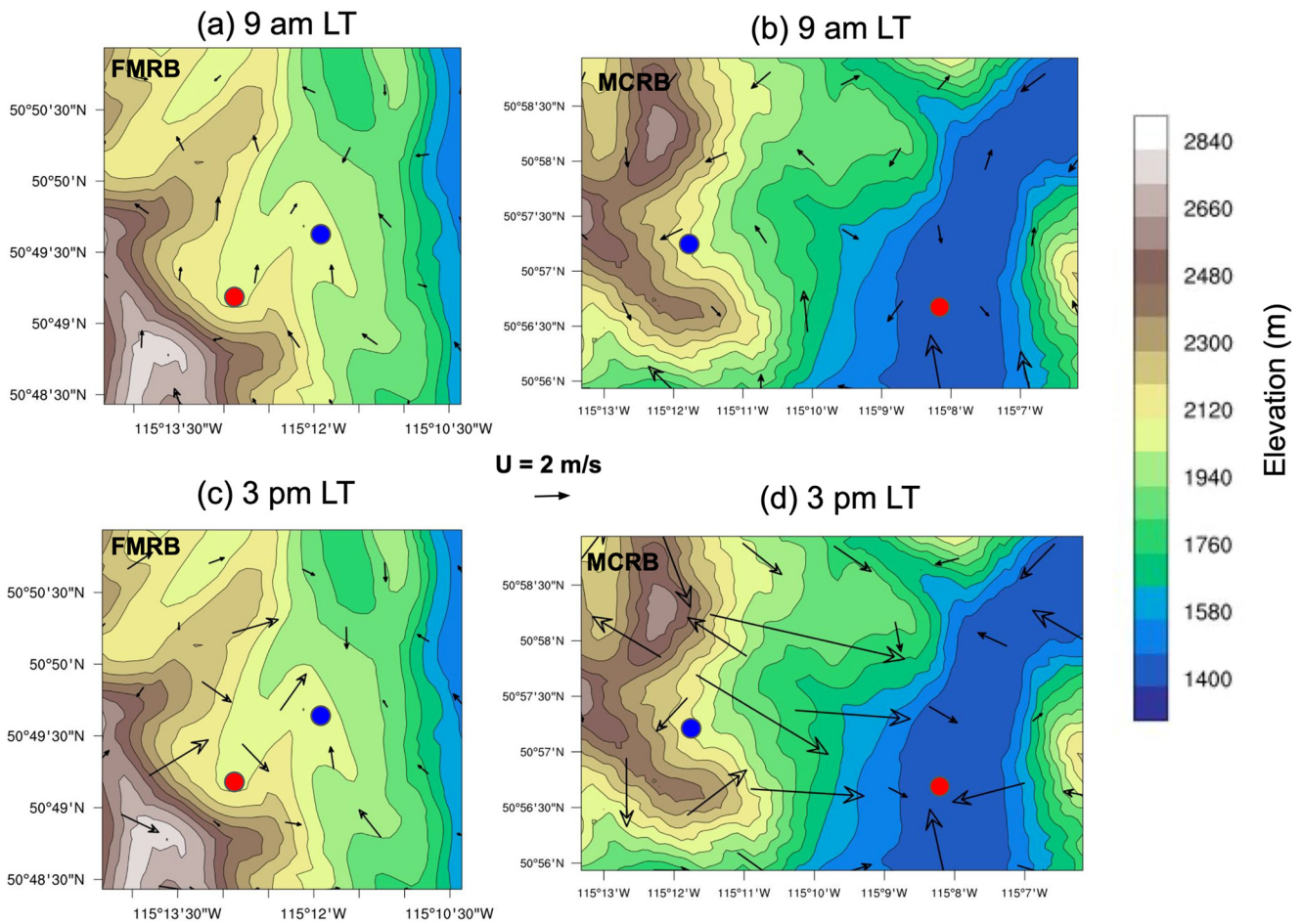
Figure 12. Surface horizontal wind vectors (at 10 m above ground level) of LESLF_shade_cloud in Fortress Mountain Research Basin (FMRB) at (a) 9 a.m. Local Time (LT), (c) 3 p.m. LT, and in Marmot Creek Research Basin (MCRB) at (b) 9 a.m. LT, and (d) 3 p.m. LT. The red dots denote the locations of valley stations (BNS and HAY), and the blue dots are the locations of ridge tops (POW and FIS) in FMRB and MCRB, respectively. The orography is shown in color, and with isolines every 90 m in the vertical.
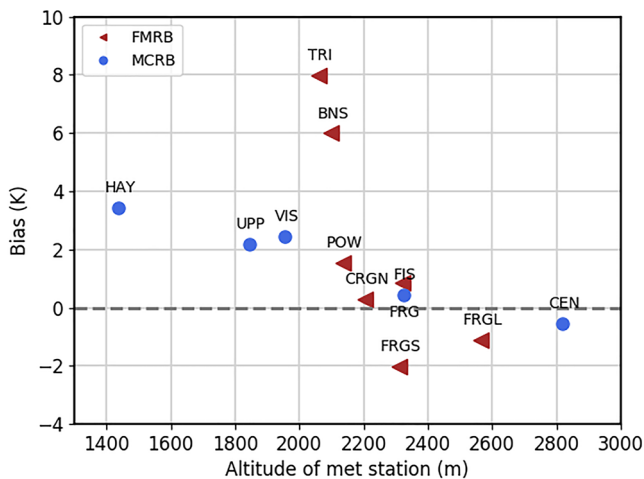

Figure 13. Nighttime (6 a.m. Local Time) 2-m air temperature LESLF_shade_cloud bias for Fortress Mountain Research Basin and Marmot Creek Research Basin stations.

Although HAY is in a wider valley (Figure 12), the presence of stronger observed up-valley wind in the afternoon at HAY (>2 m/s) (Figure 9a) in MCRB when compared to BNS in FMRB (<2 m/s) (Figure 8a), can suggest that valley depth is more important than width in influencing winds in this study. However, it is not possible to make a definite conclusion about the impact of valley geometry since valley orientation and its effect on solar heating of slopes is another important factor in the formation of valley flows.

The overall topography of the terrain seem to influence the performance of the smoothing methods. The simulated wind speed in Figures 8 and 9 showed differences caused by LESGF and local filtering simulations at the valley locations. The effect of filtering techniques and overall sensitivity simulation seems to be larger at the wider valley (HAY) than the narrower valley (BNS) in the simulations.

Topographic differences between FMRB and MCRB can cause differences in model temperature bias. The nighttime warm bias at 6 a.m. for individual stations revealed a correlation between elevation and temperature bias (Figure 13). Lower altitude stations below 2,200 m AGL in FMRB, and below 2,300 m in MCRB showed a warm bias while above 2,300 m showed
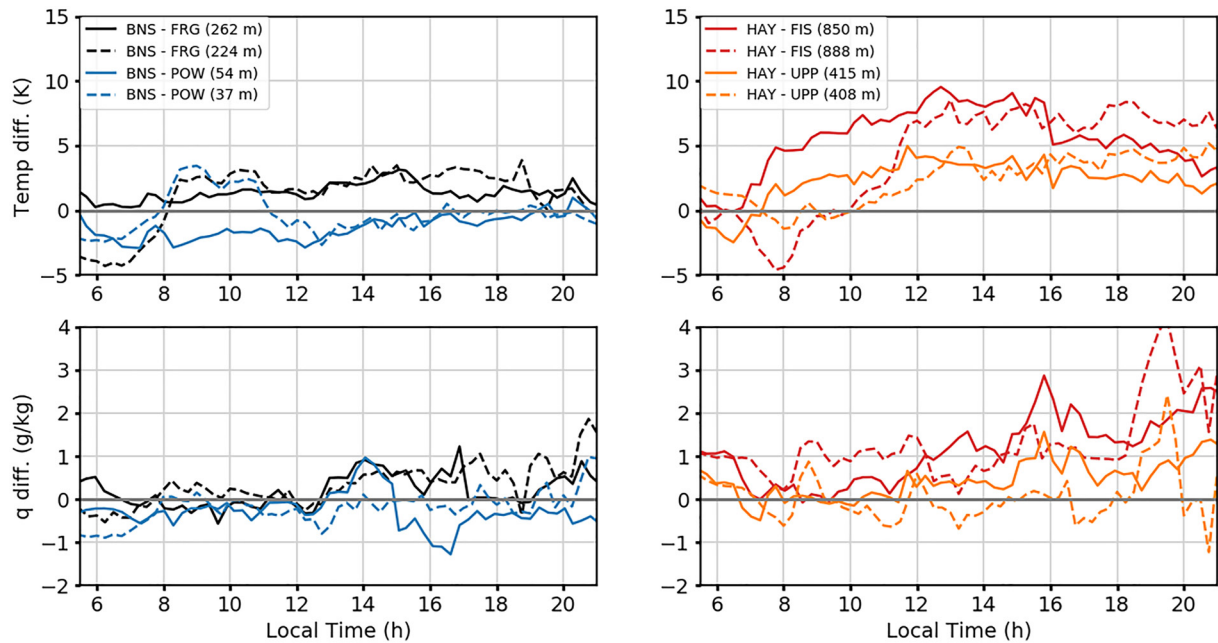
Figure 14. 2-m air temperature and specific humidity differences for pairs of valley and ridge top stations in Fortress Mountain Research Basin and Marmot Creek Research Basin for LESLF_shade_cloud (solid lines) and observations (dashed lines). Model and actual elevation differences for a pair of sites are given for reference.

a cold bias. The warm bias rose more rapidly for FMRB at the lower elevations as compared to MCRB. As discussed, cold-air pool seemed to linger longer in the deeper and wider valley at MCRB (Figure 10c), but temperatures were lower near the morning at the FMRB valley location (Figure 10a), likely due to the narrower valley with more topographic shading. The 6 a.m. air temperature at the lowest valley station in FMRB (TRI) was −2.5°C, while it was 5.6°C at HAY in MCRB. Consequently, nighttime model biases were larger for FMRB valley locations, and rose faster with descend in elevation.

Figure 14 illustrates daily differences in the simulated (LESLF_shade_cloud) and the observed absolute magnitude of temperature and specific humidity for a pair of locations, with different elevations in FMRB and MCRB. The largest differences in nighttime (before 8 a.m.) temperatures between the simulations and observations were for the sites BNS and FRG (valley and ridge top in FMRB) with model and actual elevation differences of 262 and 224 m, respectively, due to a larger cold-air pool effect, as compared to a pair of valley and ridge top, BNS and POW, which differed less in elevation (54 and 37 m). Similarly, valley and ridge top (HAY and FIS) in MCRB mountain range displayed larger differences in cold-air pool bias than HAY and mid-altitude ridge top (UPP) with less elevation differences. The bias between simulations and observations diminished faster in FMRB since the observed cold-air pool effect diminished earlier in FMRB (Figure 10).

The simulations conducted over both the MCRB and FMRB areas revealed that specific humidity was overestimated during daytime, which peaked in the afternoon with the increase in air instability with a maximum of 6 and 4 g/kg for MCRB and FMRB stations, respectively. The insensitivity of model predictions to humidity differences in altitude or location of forecast is similar to temperature bias, and could be related to the model's inability to properly simulate horizontal mixing of air temperature and moisture in steep terrain (Zängl, 2002).

The magnitude of humidity bias was found to be correlated with elevation, with the model's overestimations of moisture tending to increase with height, as reported by Doyle et al. (2013). Moreover, the simulated and observed differences in humidity after sunrise were more pronounced in MCRB than in FMRB for a pair of sites, likely due to lager elevation differences between the MCRB sites. This indicates that the model has more difficulty predicting moisture on ridge tops than in valleys, particularly in a deeper and wider mountain valley.

4. Summary and Conclusions

In this paper, the performance of high-resolution LES to resolve thermally driven flows, and near-surface boundary layer characteristics of mountainous terrain in Canadian Rockies with two different methods of global and

local terrain smoothing were examined. Simulations were performed for two summer days with different synoptic conditions, for which rare sounding profiles were available. Predictions were also evaluated using data from automatic stations, located at a variety of elevations for valleys and ridge tops in two mountain basins with different valley sizes and volumes. Forecasts were provided for 18 July 2016, at 90 m horizontal resolution for LES results and were compared against a mesoscale model at 180 m grid spacing.

Evaluations of vertical profiles of wind speed and direction using SODAR measurements demonstrate improved predictions for wind direction by the LES, which utilized local filtering smoothing, topographic shading, and cumulus parametrization activated only for the parent domain to avoid the gray zone (LESLF_shade_cloud). Time series evolution of wind speed at 40 m AGL shows better agreement with the observed afternoon rise in turbulent fluctuations for LES versus mesoscale, while time series of wind direction presents the lowest RMSE for LESLF_shade_cloud, and the highest RMSE for LESGF compared to all the local filtering simulations. Overall, daily evolution and error statistics at valley and ridge top locations for surface wind, air temperature, and humidity show similar performance for all the LES and mesoscale simulations. However, the local filtering simulation, LESLF_shade_cloud, with the cumulus parametrization activated only for the parent domain provides better predictions for surface wind direction, improved predictions for net radiation, and better RMSE for humidity. Hence, LESLF_shade_cloud is a preferable model compared to the other tested simulations to study the boundary layer processes in this study.

LES wind forecasts are consistent with the findings of other mountain studies (e.g., Goger et al., 2022; Liu et al., 2020; Umek et al., 2021). But this assessment also highlights that correct topographic representation, and radiation in very complex terrain has a crucial role in model predictions. For better evaluation of various smoothing methodologies, higher resolution simulations and other methods dealing with terrain following coordinates with more refined vertical grid nesting should be considered for future work.

Flow reversals, topographic and mesoscale winds can all have important influences on thermally driven wind flows in complex terrain. The simulated wind direction had difficulty following observations in the valley locations, and the wind switched between up-valley and down-valley in some instances in the afternoon hours. In this study, both cloud shading and wind gusts seem to contribute to short-lived flow reversals at the valley locations.

Larger errors in nighttime and early morning air temperatures reveal that the simulations in this study underestimated cold-air pool effects, and underpredicted air temperature during the warmer convective hours in mid-day. One possible reason for this discrepancy is faster cooling by clouds in the model compared to reality. Interestingly, nighttime cold-air pool bias decreased toward the higher elevations, indicating an elevation dependency of the value of nightitme cold bias. Specifically, the nighttime cold bias became greater toward the lower elevations for both mountain basins in the study. The elevation dependency was more pronounced for FMRB, which has a narrower valley area, than for MCRB. This difference could be due to a larger drop in observed nighttime temperatures in the narrower valley of FMRB with more topographic shading. In contrast, the removal of cold-air pool due to temperature rise happened earlier in the valley in FMRB than in the valley of MCRB due to an elevated inversion layer of the deeper valley. Moreover, the up-valley flows were stronger in the wide but deeper Kananaskis Valley in MCRB, as compared to the narrower and shallower valley in FMRB. In this study, the larger valley volume has an impact on up-valley wind strength. The formation and transition of down-valley to up-valley occurred earlier in MCRB valley than in FMRB valley. This is a complex process in a complex terrain, and could be related to a combination of various factors such as the thermodynamics related to valley geometry and orientation, contribution from upslope flows, and the rate at which cold air drains down the valley, which helps with the formation of up-valley flows.

This study also illustrates the shortcomings in model predictions of LES for daytime thermally driven wind flow in alpine terrain, and demonstrates the improvement of high-resolution LES with correct cloud shading in predictions of diurnal radiative fluxes and wind flow patterns. Improvement in high-resolution numerical modeling of diurnal wind flows and radiation in complex terrain is essential in calculation of water vapor and heat fluxes and exchange processes in surface-atmosphere interactions in mountain terrain. The improvement in representation of topography and land cover combined with multiscale simulations at high-resolution can help broaden our scope of weather forecasting and predictions of boundary layer processes in mountain basins.

Earth and Space Science

Data Availability Statement

Station data, SODAR raw and processed data, and example scripts in Python for the corresponding figures of this article have been shared at https://doi.org/10.5281/zenodo.8377356 (Rohanizadegan et al., 2023).

References

Arnold, D., Morton, D., Schicker, I., Seibert, P., Rotach, M., Horvath, K., et al. (2012). High resolution modelling in complex terrain. In *Report on the HiRCOT 2012 workshop*. Institut für Meteorologie, Department Wasser-Atmosphäre-Umwelt, Univ. f. Bodenkultur.

Arthur, R. S., Lundquist, K. A., Mirocha, J. D., & Chow, F. K. (2018). Topographic effects on radiation in the WRF model with the immersed boundary method: Implementation, validation, and application to complex terrain. *Monthly Weather Review*, *146*(10), 3277–3292. https://doi.org/10.1175/mwr-d-18-0108.1

Chow, F. K., Schär, C., Ban, N., Lundquist, K. A., Schlemmer, L., & Shi, X. (2019). Crossing multiple gray zones in the transition from mesoscale to microscale simulation over complex terrain. *Atmosphere*, *10*(5), 274. https://doi.org/10.3390/atmos10050274

Chow, F. K., Weigel, A. P., Street, R. L., Rotach, M. W., & xue, M. (2006). High-resolution large-eddy simulations of flow in a steep alpine valley. part I: Methodology, verification, and sensitivity experiments. *Journal of Climate and Applied Meteorology*, *45*(1), 63–86. https://doi.org/10.1175/jam2322.1

Chow, F. K., Wekker, S. F. D., & Snyder, B. J. (2013). *Mountain weather research and forecasting: Recent progress and current challenges*. Springer.

Conway, J. P., Pomeroy, J. W., Helgason, W. D., & Kinar, N. J. (2018). Challenges in modeling turbulent heat fluxes to snowpacks in forest clearings. *Journal of Hydrometeorology*, *19*(10), 1599–1616. https://doi.org/10.1175/jhm-d-18-0050.1

Cuxart, J. (2015). When can a high-resolution simulation over complex terrain be called LES? *Frontiers in Earth Science*, *3*, 87. https://doi.org/10.3389/feart.2015.00087

Daniels, M. H., Lundquist, K. A., Mirocha, J. D., Wiersema, D. J., & Chow, F. K. (2016). A new vertical grid nesting capability in the weather research and forecasting (WRF) model. *Monthly Weather Review*, *144*(10), 3725–3747. https://doi.org/10.1175/mwr-d-16-0049.1

Dee, D., Uppala, S. M., Simmons, A. J., Berrisford, P., Poli, P., Kobayashi, S., et al. (2011). The era-interim reanalysis: Configuration and performance of the data assimilation system. *Quarterly Journal of the Royal Meteorological Society*, *137*(656), 553–597. https://doi.org/10.1002/qj.828

Doyle, J. D., Epifanio, C. C., Persson, A., Reinecke, P. A., & Zängl, G. (2013). Mesoscale modeling over complex terrain: Numerical and predictability perspectives. In *Mountain weather research and forecasting* (pp. 531–589).

Dudhia, J. (1989). Numerical study of convection observed during the winter monsoon experiment using a mesoscale two-dimensional model. *Journal of the Atmospheric Sciences*, *46*(20), 3077–3107. https://doi.org/10.1175/1520-0469(1989)046<3077:nsocod>2.0.co;2

Fang, X., Pomeroy, J. W., Ellis, C. R., MacDonald, M. K., DeBeer, C. M., & Brown, T. (2013). Multi-variable evaluation of hydrological model predictions for a headwater basin in the Canadian rocky mountains. *Hydrology and Earth System Sciences*, *17*(4), 1635–1659. https://doi.org/10.5194/hess-17-1635-2013

Fillion, L., Tanguay, M., Lapalme, E., Denis, B., Desgagne, M., Lee, V., et al. (2010). The Canadian regional data assimilation and forecasting system. *Weather and Forecasting*, *25*(6), 1645–1669. https://doi.org/10.1175/2010waf2222401.1

Gerber, F., Besic, N., Sharma, V., Mott, R., Daniels, M., Gabella, M., et al. (2018). Spatial variability in snow precipitation and accumulation in COSMO–WRF simulations and radar estimations over complex terrain. *The Cryosphere*, *12*(10), 3137–3160. https://doi.org/10.5194/tc-12-3137-2018

Goger, B., Rotach, M. W., Gohm, A., Fuhner, O., Stiperski, I., & Holstag, A. A. M. (2018). The impact of three-dimensional effects on the simulation of turbulence kinetic energy in a major alpine valley. *Boundary-Layer Meteorology*, *168*, 1–27. https://doi.org/10.1007/s10546-018-0341-y

Goger, B., Stiperski, I., Nicholson, L., & Sauter, T. (2022). Large-eddy simulations of the atmospheric boundary layer over an alpine glacier: Impact of synoptic flow direction and governing processes. *Quarterly Journal of the Royal Meteorological Society*, *148*(744), 1319–1343. https://doi.org/10.1002/qj.4263

Golzio, A., Ferrarese, S., Cassardo, C., Diolaiuti, G. A., & Pelfini, M. (2021). Land-use improvements in the weather research and forecasting model over complex mountainous terrain and comparison of different grid sizes. *Boundary-Layer Meteorology*, *180*(2), 319–351. https://doi.org/10.1007/s10546-021-00617-1

Harder, P., Schirmer, M., Pomeroy, J., & Helgason, W. (2016). Accuracy of snow depth estimation in mountain and prairie environments by an unmanned aerial vehicle. *The Cryosphere*, *10*(6), 2559–2571. https://doi.org/10.5194/tc-10-2559-2016

Helgason, W., & Pomeroy, J. W. (2012). Characteristics of the near-surface boundary layer within a mountain valley during winter. *Journal of Climate and Applied Meteorology*, *51*(3), 583–597. https://doi.org/10.1175/jamc-d-11-058.1

Hogstrom, U. (1990). Analysis of turbulence structure in the surface layer with a modified similarity formulation for near neutral conditions. *Journal of the Atmospheric Sciences*, *47*(16), 1949–1971. https://doi.org/10.1175/1520-0469(1990)047<1949:aotsit>2.0.co;2

Hong, S.-Y., Noh, Y., & Dudhia, J. (2006). A new vertical diffusion package with an explicit treatment of entrainment processes. *Monthly Weather Review*, *134*(9), 2318–2341. https://doi.org/10.1175/mwr3199.1

Janjić, Z. I. (1994). The step-mountain eta coordinate model: Further developments of the convection, viscous sublayer, and turbulence closure schemes. *Monthly Weather Review*, *122*(5), 927–945. https://doi.org/10.1175/1520-0493(1994)122<0927:tsmecm>2.0.co;2

Jeworrek, J., West, G., & Stull, R. (2019). Evaluation of cumulus and microphysics parametrizations in WRF across the convective gray zone. *Weather and Forecasting*, *34*(4), 1097–1115. https://doi.org/10.1175/waf-d-18-0178.1

Jiménez, P. A., & Dudhia, J. (2012). Improving the representation of resolved and unresolved topographic effects on surface wind in the WRF model. *Journal of Applied Meteorology and Climatology*, *51*(2), 300–316. https://doi.org/10.1175/jamc-d-11-084.1

Jiménez, P. A., Dudhia, J., González-Rouco, J. F., Navarro, J., Montávez, J. P., & García-Bustamante, E. (2012). A revised scheme for the WRF surface layer formulation. *Monthly Weather Review*, *140*(3), 898–918. https://doi.org/10.1175/mwr-d-11-00056.1

Jimenez-Esteve, B., Udina, M., Soler, M. R., Pepin, N., & Miro, J. R. (2018). Land use and topography influence in a complex terrain area: A high resolution mesoscale modelling study over the Eastern Pyrenees using the WRF model. *Atmospheric Research*, *202*, 49–62. https://doi.org/10.1016/j.atmosres.2017.11.012

Kaimal, J. C., & Finnigan, J. J. (1994). *Atmospheric boundary layer flows: Their structure and measurement*. Oxford Univ. Press.

Kain, J. S. (2004). The Kain-Fritsch convective parametrization: An update. *Journal of Applied Meteorology*, *43*(1), 170–181. https://doi.org/10.1175/1520-0450(2004)043<0170:tkcpau>2.0.co;2

Kalverla, P., Duine, G.-J., Steeneveld, G.-J., & Hedde, T. (2016). Evaluation of the weather research and forecasting model in the durance valley complex terrain during the Kascade field campaign. *Journal of Applied Meteorology and Climatology*, *55*(4), 861–882. https://doi.org/10.1175/jamc-d-15-0258.1

Kirkil, G., Mirocha, J., BouZeid, E., Chow, F. K., & Kosovic, B. (2012). Implementation and evaluation of dynamic subfilter scale stress models for large-eddy simulation using WRF. *Monthly Weather Review*, *140*(1), 266–284. https://doi.org/10.1175/mwr-d-11-00037.1

Klemp, J. B., Skamarock, W. C., & Dudhia, J. (2007). Conservative split-explicit time integration methods for the compressible nonhydrostatic equations. *Monthly Weather Review*, *135*(8), 2897–2913. https://doi.org/10.1175/mwr3440.1

Knievel, J. C., Bryan, G. H., & Hacker, J. P. (2007). Explicit numerical diffusion in the WRF model. *Monthly Weather Review*, *135*(11), 3808–3824. https://doi.org/10.1175/2007mwr2100.1

Kosović, B. (2020). Wps-geo-localfilter.v1.0. *GitHub*. https://doi.org/10.5281/zenodo.4083750

Lehner, M., & Rotach, M. (2018). Current challenges in understanding and predicting transport and exchange in the atmosphere over mountainous terrain. *Journal of Atmosphere*, *9*(7), 276. https://doi.org/10.3390/atmos9070276

Lilly, K. (1966). On the application of the eddy viscosity concept in the inertial sub-range of turbulence. *NCAR Manuscr*, *123*, 19.

Lilly, K. (1967). The representation of small-scale turbulence in numerical simulation experiments. In *IBM Scientific Computing Symposium on Environmental Sciences* (pp. 195–210).

Liu, Y., Liu, Y., Muñoz-Esparza, D., Hu, F., Yan, C., & Miao, S. (2020). Simulation of flow fields in complex terrain with WRF-LES: Sensitivity assessment of different PBL treatments. *Journal of Applied Meteorology and Climatology*, *59*(9), 1481–1501. https://doi.org/10.1175/jamc-d-19-0304.1

Mesinger, F., DiMego, G., Kalnay, E., Mitchell, K., Shafran, P. C., Ebisuzaki, W., et al. (2006). North American regional reanalysis. *Bulletin of the American Meteorological Society*, *87*(3), 343–360. https://doi.org/10.1175/bams-87-3-343

Mirocha, J., Kosović, B., & Kirkil, G. (2014). Resolved turbulence characteristics in large-eddy simulations nested within mesoscale simulations using the weather research and forecasting model. *Monthly Weather Review*, *142*(2), 806–831. https://doi.org/10.1175/mwr-d-13-00064.1

Mlawer, E. J., Taubman, S. J., Brown, P. D., Iacono, M. J., & Clough, S. A. (1997). Radiative transfer for inhomogeneous atmospheres: RRTM, a validated correlated-k model for the longwave. *Journal of Geophysical Research*, *102*(D14), 16663–16682. https://doi.org/10.1029/97jd00237

Moeng, C. H., Dudhia, J., Klemp, J., & Sullivan, P. (2007). Examining two-way grid nesting for large eddy simulation of the PBL using the WRF model. *Monthly Weather Review*, *135*(6), 2295–2311. https://doi.org/10.1175/mwr3406.1

Monin, A. S., & Obukhov, A. M. (1954). *Basic turbulent mixing laws in the atmospheric surface layer* (Vol. 24, pp. 163–187). Trudy Geofiz. Inst. Akad. Nauk SSSR.

Muñoz-Esparza, D., Kosović, B., Beeck, J. V., & Mirocha, J. (2015). A stochastic perturbation method to generate inflow turbulence in large-eddy simulation models: Application to neutrally stratified atmospheric boundary layers. *Physics of Fluids*, *27*(3), 035102. https://doi.org/10.1063/1.4913572

Muñoz-Esparza, D., Kosović, B., Mirocha, J., & van Beeck, J. (2014). Bridging the transition from mesoscale to microscale turbulence in numerical weather prediction models. *Boundary-Layer Meteorology*, *153*(3), 409–440. https://doi.org/10.1007/s10546-014-9956-9

Muñoz-Esparza, D., Lundquist, J. K., Sauer, J. A., Kosović, B., & Linn, R. R. (2017). Coupled mesoscale-les modeling of a diurnal cycle during the CWEX-13 field campaign: From weather to boundary-layer eddies. *Journal of Advances in Modeling Earth Systems*, *9*(3), 1572–1594. https://doi.org/10.1002/2017ms000960

Muñoz-Esparza, D., Sauer, J. A., Lin, R. R., & Kosović, B. (2016). Limitations of one-dimensional mesoscale PBL parameterizations in reproducing mountain-wave flows. *Journal of the Atmospheric Sciences*, *73*(7), 2603–2614. https://doi.org/10.1175/jas-d-15-0304.1

Nakanishi, M., & Niino, H. (2006). An improved Mellor–Yamada level-3 model: Its numerical stability and application to a regional prediction of advection fog. *Boundary-Layer Meteorology*, *119*(2), 397–407. https://doi.org/10.1007/s10546-005-9030-8

Niu, G.-Y., Yang, Z.-L., Mitchell, K. E., Chen, F., Ek, M. B., Barlage, M., et al. (2011). The community Noah land surface model with multiparameterization options (Noah-MP): 1. Model description and evaluation with local-scale measurements. *Journal of Geophysical Research*, *116*(D12), D12109. https://doi.org/10.1029/2010jd015139

Pagès, M., Pepin, N., & Miró, J. R. (2017). Measurement and modelling of temperature cold pools in the C erdanya valley (Pyrenees), Spain. *Meteorological Applications*, *24*(2), 290–302. https://doi.org/10.1002/met.1630

Rai, R. K., Berg, L. K., Kosović, B., Mirocha, J. D., Pekour, M. S., & Shaw, W. J. (2017). Comparison of measured and numerically simulated turbulence statistics in a convective boundary layer over complex terrain. *Boundary-Layer Meteorology*, *163*(1), 69–89. https://doi.org/10.1007/s10546-016-0217-y

Rohanizadegan, M., Petrone, R., Pomeroy, J., Kosovic, B., Munoz-Esparza, D., & Helgason, W. (2023). High resolution large-eddy simulations of flow in the complex terrain of the Canadian Rockies (version v2023-09-25-v2). [Dataset]. https://doi.org/10.5281/zenodo.8377356

Rotach, M. W., Gohm, A., Lang, M. N., Leukauf, D., Stiperski, I., & Wagner, J. S. (2015). On the vertical exchange of heat, mass, and momentum over complex, mountainous terrain. *Frontiers in Earth Science*, *3*, 76. https://doi.org/10.3389/feart.2015.00076

Schmidli, J., & Rotunno, R. (2010). Mechanisms of along-valley winds and heat exchange over mountainous terrain. *Journal of the Atmospheric Sciences*, *67*(9), 3033–3047. https://doi.org/10.1175/2010jas3473.1

Serafin, S., Adler, B., Cuxart, J., De Wekker, S., Gohm, A., Grisogono, B., et al. (2018). Exchange processes in the atmospheric boundary layer over mountainous terrain. *Atmosphere*, *9*(3), 102. https://doi.org/10.3390/atmos9030102

Sertel, E., Robock, A., & Ormeci, C. (2010). Impacts of land cover data quality on regional climate simulations. *International Journal of Climatology*, *30*(13), 1942–1953. https://doi.org/10.1002/joc.2036

Skamarock, W. C., Klemp, J. B., Dudhia, J., Gill, D. O., Barker, D. M., Duda, M. G., et al. (2008). A description of the advanced research WRF version 3. NCAR technical note.

Smagorinsky, J. (1963). General circulation experiments with the primitive equations: I. The basic experiment. *Monthly Weather Review*, *91*(3), 99–164. https://doi.org/10.1175/1520-0493(1963)091<0099:gcewtp>2.3.co;2

Sukoriansky, S., Galperin, B., & Perov, V. (2005). Application of a new spectral theory of stably stratified turbulence to the atmospheric boundary layer over sea ice. *Boundary-Layer Meteorology*, *117*(2), 231–257. https://doi.org/10.1007/s10546-004-6848-4

Udina, M., Soler, M. R., & Sol, O. (2017). A modeling study of a trapped lee-wave event over the Pyrénées. *Monthly Weather Review*, *145*(1), 75–96. https://doi.org/10.1175/mwr-d-16-0031.1

Umek, L., Gohm, A., Haid, M., Ward, H. C., & Rotach, M. W. (2021). Large eddy simulation of foehn-cold pool interactions in the Inn Valley during PIANO IOP2. *Quarterly Journal of the Royal Meteorological Society*, *147*(735), 944–982. https://doi.org/10.1002/qj.3954

Umek, L., Gohm, A., Haid, M., Ward, H. C., & Rotach, M. W. (2022). Influence of grid resolution of large-eddy simulations on foehn-cold pool interaction. *Quarterly Journal of the Royal Meteorological Society*, *148*(745), 1840–1863. https://doi.org/10.1002/qj.4281

Vionnet, V., Belair, S., Girard, C., & Plante, A. (2015). Wintertime subkilometer numerical forecasts of near-surface variables in the Canadian rocky mountains. *Monthly Weather Review*, *143*(2), 666–686. https://doi.org/10.1175/mwr-d-14-00128.1

Wagner, J. S., Gohm, A., & Rotach, M. W. (2015). The impact of valley geometry on daytime thermally driven flows and vertical transport processes. *Quarterly Journal of the Royal Meteorological Society*, *141*(690), 1780–1794. https://doi.org/10.1002/qj.2481

Weigel, A. P., Chow, F. K., & Rotach, M. W. (2007). On the nature of turbulent kinetic energy in a steep and narrow alpine valley. *Boundary-Layer Meteorology*, *123*(1), 177–199. https://doi.org/10.1007/s10546-006-9142-9

Whiteman, C. D. (2000). *Mountain meteorology: Fundamentals and applications*. Oxford University Press.

Wiersema, D. J., Lundquist, K. A., & Chow, F. K. (2020). Mesoscale to microscale simulations over complex terrain with the immersed boundary method in the weather research and forecasting model. *Monthly Weather Review*, *148*(2), 577–595. https://doi.org/10.1175/mwr-d-19-0071.1

Wyngaard, J. C. (1973). On the surface-layer turbulence. In *In workshop on micrometeorology* (pp. 101–149).

Wyngaard, J. C. (2004). Toward numerical modeling in the "terra incognita". *Journal of the Atmospheric Sciences*, *61*(14), 1816–1826. https://doi.org/10.1175/1520-0469(2004)061<1816:tnmitt>2.0.co;2

Zängl, G. (2002). An improved method for computing horizontal diffusion in a sigma-coordinate model and its application to simulations over mountainous topography. *Monthly Weather Review*, *130*(5), 1423–1432. https://doi.org/10.1175/1520-0493(2002)130<1423:aimfch>2.0.co;2

Zardi, D., & Whiteman, C. D. (2013). Diurnal mountain wind systems. In *Mountain weather research and forecasting* (pp. 35–119). Springer.

Zhang, H., Pu, Z., & Zhang, X. (2013). Examination of errors in near-surface temperature and wind from WRF numerical simulations in regions of complex terrain. *Weather and Forecasting*, *28*(3), 893–914. https://doi.org/10.1175/waf-d-12-00109.1

Zhou, B., & Chow, F. K. (2014). Nested large-eddy simulations of the intermittently turbulent stable atmospheric boundary layer over real terrain. *Journal of the Atmospheric Sciences*, *71*(3), 1021–1039. https://doi.org/10.1175/jas-d-13-0168.1